Optical Characterization of Human Tissues Using Low Coherence Interferometry

by

Guillermo James Tearney

B.S., Applied Mathematics
Harvard University, 1988

Submitted to the

DEPARTMENT OF ELECTRICAL ENGINEERING AND COMPUTER SCIENCE

in partial fulfillment of the requirements for the degree of

MASTER OF SCIENCE

at the

MASSACHUSETTS INSTITUTE OF TECHNOLOGY

January 1995

Signature of Author _____
Department of Electrical Engineering and Computer Science
January 26, 1995

Certified by _____
Professor James G. Fujimoto
Thesis Supervisor

Accepted by _____
Frederic R. Morgenthaler
Chairman, Department Committee on Graduate Students

Optical Characterization of Human Tissues Using Low Coherence Interferometry

by
Guillermo James Tearney

Submitted to the Department of Electrical Engineering and Computer Science on January 26, 1995 in partial fulfillment of the requirements for the degree of Master of Science

Abstract

The goal of this thesis is to investigate the use of low coherence interferometry for determining the refractive index and optical properties of human tissue. The techniques described in this work will not only be useful for researchers interested in applications of optics in medicine, but will provide a foundation for understanding images obtained using low coherence interferometry. In addition, the results of the studies performed will lead to an empirical determination of the multiple scattering limits of low coherence interferometry in tissue.

Optical Coherence Tomography (OCT) is a new technique that uses low coherence interferometry to gate out multiply scattered photons, and in the single scattering limit, is equivalent to time-of-flight imaging. For an interferometric signal to be detected, the optical pathlengths of the object and reference beam must be matched to within the coherence length of the source. Since multiply scattered photons from the object have traveled different optical pathlengths than the reference beam, multiple scattering effects are minimized in the OCT image.

Techniques based on OCT have been used to measure the refractive index of *in vitro* human tissue. Tissue refractive index is determined using OCT by measuring the change in the optical pathlengths between the reference and sample arms due to the insertion of the sample. In addition, OCT enhanced confocal microscopy is used to measure the refractive index of tissue by tracking the focal position as the sample is scanned through the focus. Refractive indices of several different tissue types obtained using these two methods are presented.

Optical properties of *in vitro* human tissue are investigated using a theoretical description of the single scattered low coherence heterodyne signal from a turbid medium. This theory enables the calculation of the radar backscattering coefficient and the total attenuation coefficient from the OCT axial reflectance profile. Single backscatter theory determination of the optical properties of several *in vitro* tissue samples are presented.

The optical properties determined from single backscatter theory are used to quantify single scattering limits of low coherence interferometry. Axial point spread functions (PSF's) as a function of depth are measured from the reflectance of a razor blade immersed in several tissue samples. The spread of the PSF as a function of depth is used to evaluate the effects of multiple scattering on the OCT signal.

Thesis supervisor: Professor James G. Fujimoto
Department of Electrical Engineering and Computer Science

Acknowledgments

I would like to thank my advisor, Professor James Fujimoto, for providing me with the opportunity to complete this work. None of this could have been accomplished without the resources of the ultrafast optics lab. Moreover, Professor Fujimoto's accessibility and willingness to offer both technical and non-technical support has been instrumental to my progress this year.

I would also like to thank Dr. R. Rox Anderson for introducing me to science and teaching me the joys of discovery. My thanks also go to Joe Izatt who not only helped me start out in OCT, but made my first year here enjoyable. Eric Swanson and his staff have been extremely helpful to me, both by providing the OCT equipment and answering technical questions. The tissue used in this research was generously provided by Dr. James Southern of the Massachusetts General Hospital.

Michael Hee played a significant part in this work by developing much of the OCT technology used in this thesis. My thanks also go out to other members of the optics group, Boris Golubovic, Brett Bouma, Steve Boppart, and Igor Bilinski for aiding me with technical issues and helping me pass the oral qualifying exams. Dr. Mark Brezinski and I have been working together for the past year. I could not have completed this thesis without Mark's clinical and scientific expertise.

In addition, I would like to express my appreciation for the unending support of my family and friends. Finally, I would like to thank my wife and best friend, Melissa. Without her patience and encouragement, I would not be here and would have never gotten this far.

Table of Contents

Chapter 1

Introduction

The goal of this thesis is to investigate the use of low coherence interferometry for determining the refractive index and optical properties of human tissue. The techniques described in this work will not only be useful for researchers interested in applications of optics in medicine, but will provide a foundation for understanding images obtained using low coherence interferometry. In addition, the results of the studies performed will lead to an empirical determination of the multiple scattering limits of low coherence interferometry in tissue.

1.1 Motivation

1.1.1 Refractive Index

Knowledge of the refractive indices of human tissues is of great importance to optical diagnosis and treatment in medicine. For example, the axial point spread function (PSF) for a standard microscope objective broadens when focusing into a sample with a different refractive index than the immersion medium[1]. Thus, the ability to obtain high resolution optical images of biological samples depends on matching the immersion medium of the microscope objective to the refractive index of tissue.

The refractive index is also directly related to the molecular composition of human tissue. For example, the water content of the stratum corneum can be

characterized by its refractive index. Water content can be used to diagnose skin diseases such as psoriasis, and determine the efficacy of topical drugs for treatment of various skin disorders. In other tissue types, determination of regions of different refractive indices may provide the key for differentiating between normal and diseased muscle, adipose, and cartilaginous tissue.

1.1.2 Optical Properties

A simple, non-invasive method for quantitatively determining the optical properties of *in vivo* tissue could have an enormous impact on the field of medical optics. Once the optical properties of tissue are known, the three-dimensional transport of light through the tissue can be predicted. Detailed knowledge of the absorption coefficient, μ_a the scattering coefficient, μ_s, and the anisotropy coefficient, g, in tissue will allow for better planning of laser treatment and surgery. For example, the ability to calculate the absorption coefficient, and thus the concentration of exogenous fluorescent dye in tissue, will enable physicians to determine the irradiant dose necessary for tumor destruction during the photodynamic therapy (PDT) of cancer. Moreover, *in vivo* quantification of the concentration of tissue endogenous chromophores is useful for both clinical diagnosis and basic science research. Finally, images of spatial variations in tissue scattering and absorption can potentially provide much insight into underlying disease processes.

1.1.3 Optical Cross-sectional Reflectance Imaging

An inexpensive optical imaging device for performing cross-sectional tissue diagnosis would greatly improve the quality of medical care. If the cross-sectional images were of micron resolution, cellular and architectural morphology could be imaged, eliminating the need for tissue biopsies. In addition, optical wavelengths in the visible and near infrared could be selected around absorption maxima of endogenous chromophores that are physiologically significant, e.g. hemoglobin. The ability to select wavelengths around absorption of chromophores would give the reflectance images functional as well as structural significance.

1.2 Low Coherence Imaging

1.2.1 Optical Coherence Tomography

Measuring spatially localized reflectance in tissue is complicated by multiple scattering. Optical Coherence Tomography (OCT) is a new technique that uses low coherence interferometry to gate out multiply scattered photons, and in the single scattering limit, is equivalent to time-of-flight imaging[2]. For an interferometric signal to be detected, the optical pathlengths of the object and reference beam must be matched to within the coherence length of the source. Since multiply scattered photons from the object have traveled different optical pathlengths than the reference beam, multiple scattering effects are minimized in the OCT image.

1.2.2 OCT Enhanced Confocal Microscopy

By increasing the numerical aperture of the object imaging lens, and effectively creating an OCT enhanced confocal microscope, the axial resolution of cross-section or *en face* OCT images are improved. OCT enhanced confocal microscopy narrows the system point spread function of the confocal microscope by multiplying the PSF defined by the coherence envelope with that of the confocal system. Also, coherent detection limits the multiple scattering contribution to the resultant confocal image. Both improvements enable OCT enhanced confocal microscopy to provide higher resolution and greater contrast than standard confocal microscopy. The removal of multiple scattering from reflectance confocal microscopy makes it possible to optically image deep into tissue. With further refinement, OCT enhanced confocal microscopy may be used for three-dimensional *in vivo* histology of human tissue.

1.3 Thesis Overview

Because of the powerful ability of low coherence interferometric methods to detect single scattered light as a function of optical depth, low coherence interferometry can be used to determine both the refractive indices and optical properties of human tissue. This thesis proposes to use OCT to measure these fundamental optical characteristics of tissue.

The tissue characteristics will in turn be used to understand reflectance cross-sectional images obtained by OCT and OCT enhanced confocal microscopy. Once a fundamental understanding of the optical characteristics of tissue is attained, OCT cross-sectional images of human tissue may be interpreted. In

addition, knowledge of the optical properties of human tissue will be used to define the single scattering limits of OCT. The single scattering limits of OCT will define the depth of cross-sectional imaging at which multiple scattering begins to affect the single scattered reflectance.

1.3.1 Thesis Outline

An OCT system that accommodates multiple sources has been constructed. The source is coupled into a single mode fiber optic Michelson interferometer. Tissue axial reflectance is obtained by varying the reference arm length and digitizing the magnitude of the demodulated interference envelope. A cross-sectional image is produced by recording axial reflectance profiles while the tissue specimen is scanned laterally.

This system has been adapted to operate as an OCT enhanced confocal microscope. The sample arm objective of the OCT enhanced confocal system has a high magnification and numerical aperture. The pinhole of the OCT enhanced confocal microscope system is the aperture of the single mode fiber of the object arm. The sample is scanned axially and laterally while the reference arm length remains matched to the focus of the sample arm. The magnitude of the interference between the two arms is digitized for each x, z scan position. Because of the coherence gating provided by the low coherence interferometer, the resultant confocal image is less affected by multiple scattering.

Techniques based on OCT and OCT enhanced confocal imaging have been used to measure the refractive index of human tissue. Tissue refractive index is determined using OCT by measuring the change in the optical pathlengths between the reference and sample arms due to the insertion of the sample. This technique requires placement of the sample on a highly reflecting surface and subsequent measurement of the axial location of the reflector through the sample. Because this method requires dissection of the tissue specimens, it is appropriate for measuring the refractive index of *in vitro* tissue samples.

In addition, OCT enhanced confocal microscopy is used to measure the refractive index of tissue by tracking the focal position as the sample is scanned through the focus. The refractive index is determined from the measured focal shift, Snell's Law, and marginal ray geometric calculations. Since this method is non-contact, it is well-suited for determination of the refractive index of *in vivo*

tissue. Refractive indices of the human skin obtained using the focus tracking method are presented.

Optical properties of *in vitro* human tissue are investigated using a theoretical description of the low coherence heterodyne signal from a collection of scatterers. This theory enables the calculation of the radar backscattering coefficient and the total attenuation coefficient from the single scattered OCT axial reflectance profile. Single backscatter theory determination of the optical properties of several *in vitro* and *in vivo* tissue samples are presented.

The optical properties determined from single backscatter theory are used to quantify single scattering limits of low coherence interferometry. Axial point spread functions are measured from the reflectance of a razor blade immersed in several tissue samples. The spread of the PSF as a function of depth is used to evaluate the effects of multiple scattering on the OCT signal. The total attenuation coefficient calculated using single backscatter theory is used to quantify the maximum single scatter imaging depth in mean free paths (MFP's).

These techniques for the characterization human tissue will be useful for understanding the nature of optical transport in human tissue. Methods for measuring the refractive index and the optical properties of tissue have many applications in the field of medical optics. Moreover, these tools provide valuable information for understanding the reflectance in OCT images. Finally, empirical determination of the single scattering limits in tissue will enable future quantification of depth dependent resolution and contrast in OCT images.

Chapter 2

Low Coherence Interferometry

A cross-sectional optical imaging device for performing noninvasive "optical biopsies" in human tissue would revolutionize the field of medical imaging. Optical biopsy may be accomplished by imaging backscattered reflectance from architectural and cellular structures within tissue. However, optical imaging of spatially localized reflectance in tissue is complicated by multiple scattering. Optical Coherence Tomography is a new technique that uses low coherence interferometry to gate out multiply scattered photons. In addition to performing as an imaging device, analysis of the OCT signal enables the determination of the optical characteristics of tissue.

2.1 Low Coherence Interferometry Systems

2.1.1 OCT System

OCT functions using low coherence optical interferometry between a reference beam and a beam which is reflected from the specimen. Precise measurements of distance are possible since interference is only observed when the path lengths of the specimen and the reference arms match to within the coherence length of the light. Tissue axial reflectance is obtained by varying the reference arm length and digitizing the magnitude of the demodulated interference envelope. A cross-sectional image is produced by recording axial reflectance profiles while the tissue specimen is scanned laterally.

The OCT system consists of a single mode fiber optic Michelson interferometer which may accommodate different, short coherence length sources (Figure 2.1). A superluminescent diode (SLD) with a center wavelength of 1300 nm and a spectral bandwidth of 50 nm is used for the experiments. The system has an axial resolution of 20 μm, transverse resolution of approximately 30 μm, an object

arm power of 100 μW, and a signal to noise ratio (SNR) of 110 dB. The total scan time depends on the image size, but ranges from 3-60 seconds.

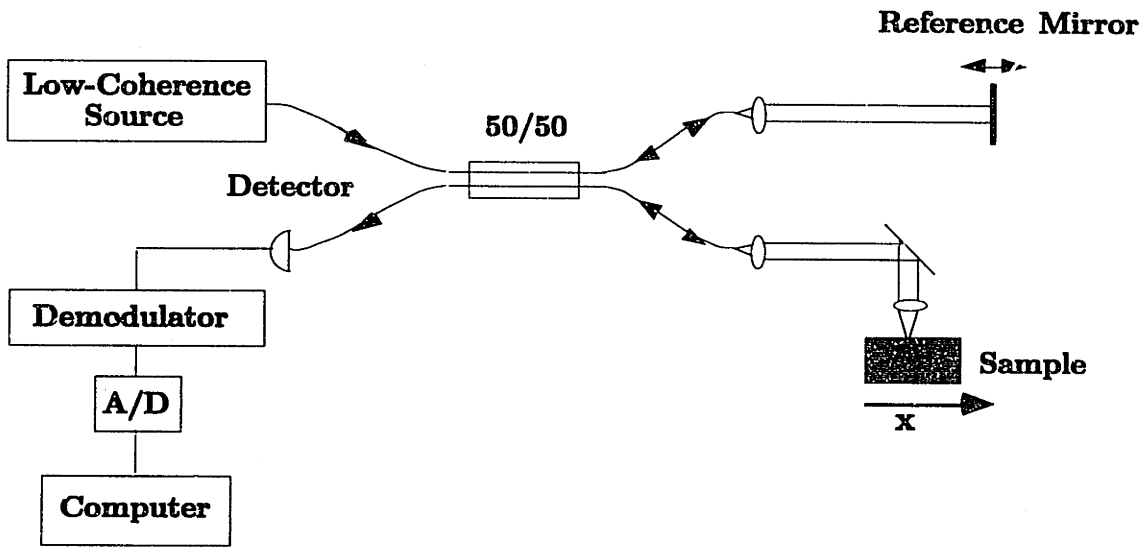

Figure 2.1. Schematic of OCT system.

2.1.2 OCT Enhanced Confocal System

A schematic of the OCT enhanced confocal microscope is shown in Figure 2.2. The OCT enhanced confocal microscope consists of broad bandwidth superluminescent diode centered at 850 nm. The coherence length of the source is approximately 20 nm. The source is coupled into a single mode fiber optic Michelson interferometer. The fiber is modulated at 20 KHz with a piezoelectric transducer and the interference signal is detected using a lock-in amplifier. The amplitude of the interferometric signal is digitized with a sampling frequency of 1 KHz, and then stored in a computer. The heterodyne detection of the OCT enhanced confocal system provides a signal to noise ratio (SNR) in excess of 110 dB. The sample arm objective has a high magnification ranging from 40x - 100x, and numerical aperture ranging from .85 - 1.3. The pinhole of the OCT enhanced confocal system is the aperture of the single mode fiber of the object arm. The sample is raster scanned axially and laterally through the focus of the objective. The image is formed from the magnitude of the interferometric signal detected at every scan position. The total image scan time ranges from 5 - 15 minutes.

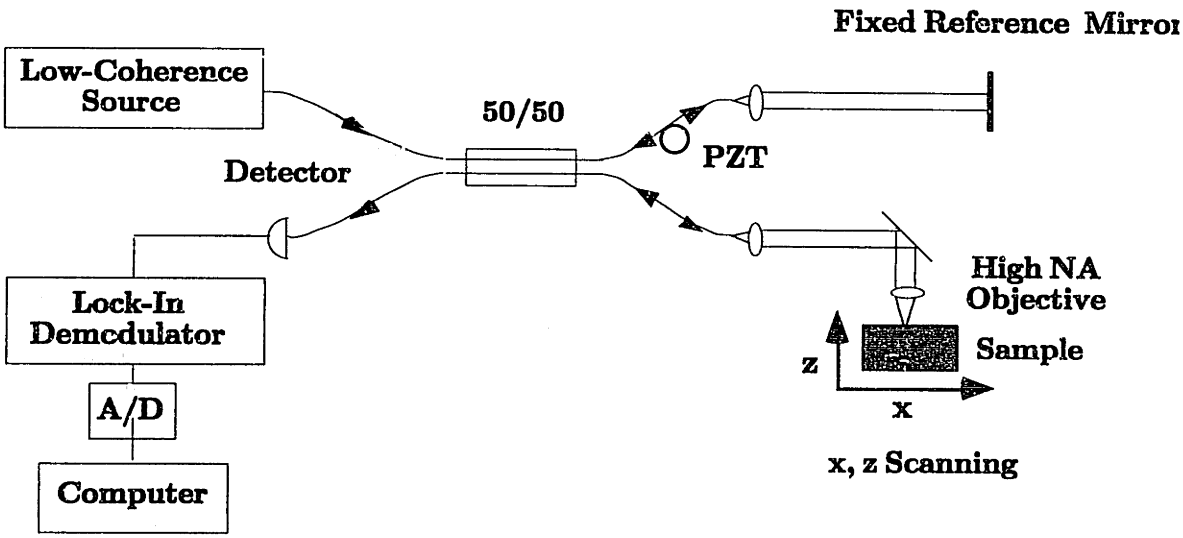

Figure 2.2. Schematic of OCT enhanced confocal microscope.

2.2 Coherence Gating Theory

2.2.1 Axial Resolution

The OCT device is a low coherence Michelson interferometer with a moving reference arm. If the illuminating radiation has a broad bandwidth and is centered around the frequency, ω_0, then the incident field amplitude can be written as:

$$a_1(t) = A_1(t)e^{j\omega_0 t}, \tag{2.2.1}$$

where $A_1(t)$ is the envelope of $a_1(t)$[3].

The photocurrent measured at the detector is determined by analyzing the two port scattering matrix of the Michelson interferometer (Figure 2.3).

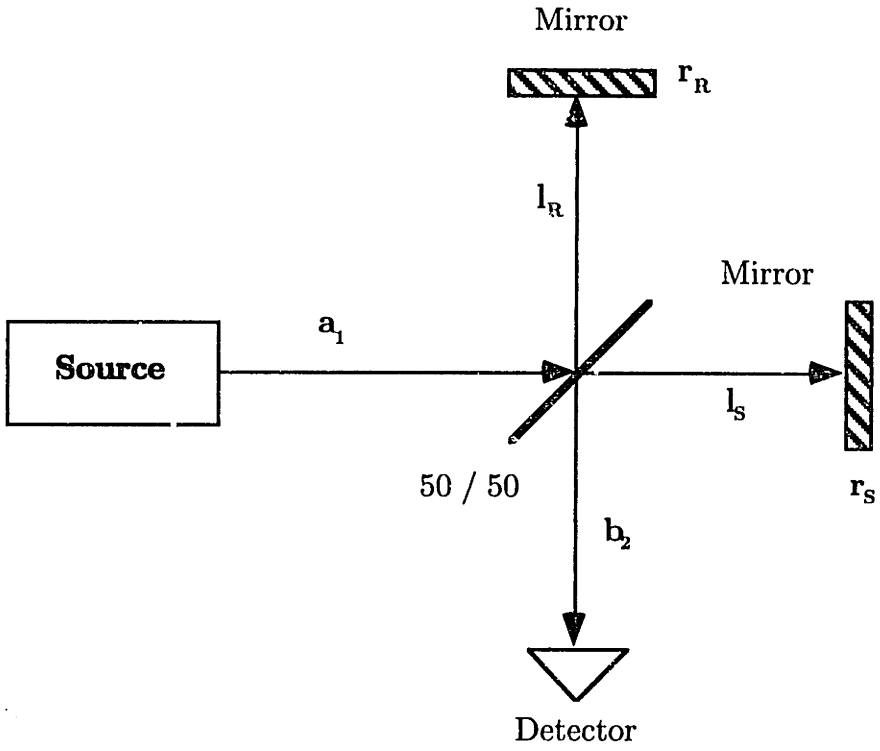

Figure 2.3. Schematic of Michelson interferometer.

Using the scattering matrix formulation for a two port system, the power at the port b_2, given a free space time delay of

$$\tau = \frac{2(l_r - l_s)}{c}, \tag{2.2.2}$$

is determined to be

$$\left\langle |b_2|^2 \right\rangle = \left[\frac{\left\langle |A_1(t)|^2 \right\rangle r_R{}^2}{4} + \frac{\left\langle |A_1(t)|^2 \right\rangle r_S{}^2}{4} + \frac{r_R r_S}{2} \left| A_1(t) A_1^*(t-\tau) \right| \cos(\omega_0 \tau) \right] \tag{2.2.3}$$

where b_2 is the output field amplitude, and r_R, r_S are the reflectivities of the reference and sample arms[3].

If the lengths of the sample and the reference arms are perfectly matched, a maximum interference signal forms at the detector. As the reference arm is moved, the magnitude of the interference signal decreases until the radiation in each arm is no longer mutually coherent. In effect, the scanning Michelson interferometer

determines temporal coherence by measuring the real part of the autocorrelation function of the source:

$$\mathrm{Re}[G(\tau)] = \frac{r_R r_S}{2}\left|A_1(t)A_1^*(t-\tau)\right|\cos(\omega_0\tau). \tag{2.2.4}$$

The autocorrelation function of the source is related to the spectral bandwidth of the source by the Wiener-Khinchin theorem:

$$S(\omega) = \frac{1}{2\pi}\int_{-\infty}^{\infty} G(\tau)\exp(-j\omega\tau)d\tau, \tag{2.2.5}$$

where ω is the optical frequency, and $S(\omega)$ is the power spectral density of the source[4].

The power spectral density of the low coherence source used in OCT can be represented by a normalized gaussian distribution in frequency:

$$S(\omega) = \sqrt{\frac{2\pi}{\sigma_\omega^2}}\exp\left(-\frac{(\omega-\omega_0)^2}{2\sigma_\omega^2}\right), \tag{2.2.6}$$

where $2\sigma_\omega$ is the standard deviation width of the gaussian distribution.

Taking the inverse Fourier transform of the spectrum of the source,

$$G(\tau) = \frac{r_R r_S}{2}\exp\left(-\frac{\tau^2\sigma_\omega^2}{2}\right)\exp(j\omega_0\tau) \tag{2.2.7}$$

and

$$\mathrm{Re}[G(\tau)] = \frac{r_R r_S}{2}\exp\left(-\frac{\tau^2\sigma_\omega^2}{2}\right)\cos(\omega_0\tau), \tag{2.2.8}$$

which is a gaussian envelope with a width of $2/\sigma_\omega$ multiplied by the carrier, $\cos(\omega_0\tau)$. The width of this gaussian autocorrelation envelope as a function of time delay or free space path length mismatch defines the axial point spread function of the OCT system.

In the OCT enhanced confocal system, the axial resolution of the imaging objective is greater than the coherence length of the light. The axial point spread function of the OCT enhanced confocal system is:

$$\hat{h}(z) = h_c(z)h_{OCT}(z) \tag{2.2.9}$$

where $h_{OCT}(z)$ is the axial PSF defined by the autocorrelation function and $\hat{h}(z)$ is the OCT enhanced confocal PSF. The confocal PSF, $h_c(z)$, is defined by:

$$h_c(z) = \left[\frac{\sin\left(kzNA^2\right)}{kzNA^2}\right], \tag{2.2.10}$$

where NA is the numerical aperture of the objective and k is the wavenumber of the source[5]. A plot of the OCT enhanced confocal PSF, computed from Equation 2.2.9, is shown in Figure 2.4.

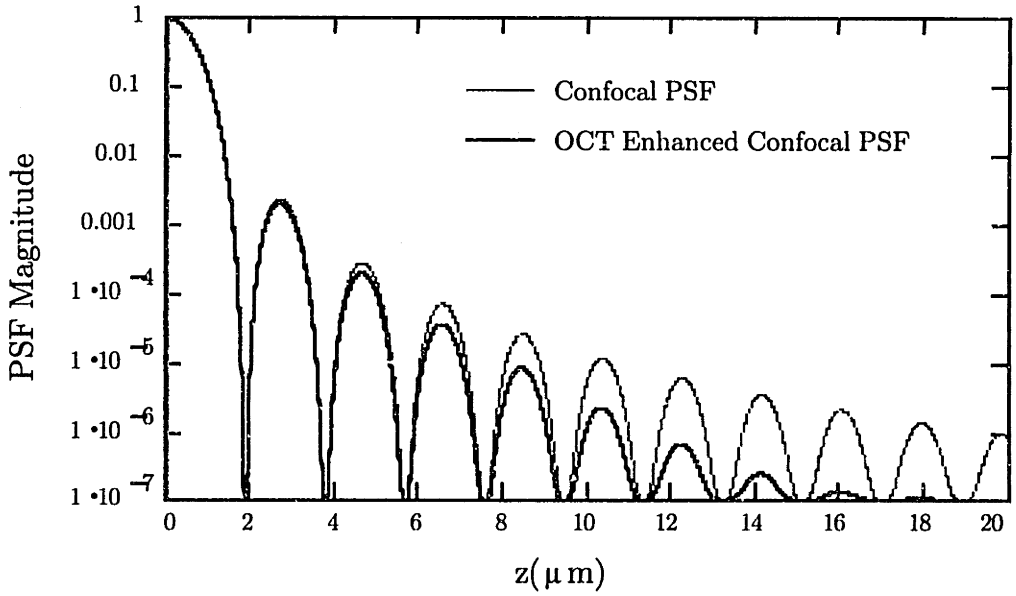

Figure 2.4. Plot of OCT enhanced confocal PSF vs. the confocal PSF. The objective specifications are 40x, 0.95 NA, no immersion fluid. The FWHM of the autocorrelation function envelope is 20 μm.

Not only does OCT enhanced confocal attenuate the sidelobes of the confocal PSF, but it also enables this PSF to be maintained over a greater penetration depth by gating out multiply scattered light.

2.2.2 Lateral Resolution

The lateral point spread function of the OCT system is determined by the imaging lens. The spot size of the lowest order mode gaussian beam produced by the imaging lens can be determined using the Fresnel diffraction formula in the paraxial limit[4]. The full-width half maximum (FWHM) of the gaussian spatial distribution, or spot diameter, D, can be calculated from the wavelength, λ, and the confocal parameter, b:

$$D = 2\sqrt{\frac{b\lambda}{\pi}}. \tag{2.2.11}$$

2.2.3 Noise in OCT images

Currently, OCT detection has been optimized to perform in the shot noise limit[6]. Shot noise arises from current fluctuations due to the conversion of light into charge. This form of noise is a wide sense stationary (WSS) stochastic process[6]. A WSS process has a constant mean. The shot noise associated with any given mean photocurrent, $\langle i \rangle$ has a constant power spectral density, commonly referred to as white noise.

In general, the shot noise power spectral density is proportional to the mean photocurrent, $\langle i \rangle$:

$$S_i(\omega) = e\langle i \rangle \tag{2.2.12}$$

where e is the electron charge and $S_i(\omega)$ is the shot noise power spectral density.

In OCT, the reference power at the detector is typically much larger than the sample power ($r_r >> r_s$). Since the reference power remains constant during the scan, the total photocurrent in the system varies only slightly about $\langle i \rangle$. Thus, the shot noise of the OCT system can be treated as additive white noise[6].

2.3 Limits of Low Coherence Interferometry

The ability of OCT to detect single scattered light in multiply scattering media has not yet been fully investigated. However, several important upper limits on the ability of OCT to image through multiply scattering media have been defined, both for coherence gated transillumination[7] and OCT enhanced confocal microscopy[8].

Using a femtosecond mode locked laser transillumination OCT system, the upper limit of ballistic or unscattered light detection has been determined to be:

$$L = \frac{1}{\mu_t} \ln\left(\frac{E}{2\hbar\omega}\right) \tag{2.2.13}$$

where $\hbar\omega$ is the energy of a single photon and L is the maximum sample thickness for ballistic imaging when the imaging detection SNR = 1[6]. According to this limit, ballistic imaging can be performed through 20 MFP's in a scattering medium[7]. However, this limit does not hold for low coherence imaging because it does not include the effects of multiply scattered coherent light reaching the detector.

Past research using heterodyne single scattered backscattered theory determined that OCT enhanced confocal microscopy has a SNR = 1 for a depth of

$$L = \frac{1}{2\mu_t}\left[\frac{\pi^2}{4n_0^2} M^2\right], \tag{2.2.14}$$

where M is the magnification of the imaging objective and n_0 is the refractive index of the medium[8]. Using this limit, the total number of MFP's that single scattering OCT enhanced confocal microscopy can image through was found to be 15-20 MFP's[8]. Since Equation 2.2.14 is obtained using single scattering theory, it is the best case limit for OCT in multiply scattering media. However, it does not consider how multiple scattering effects the resolution as a function of depth. This issue will be addressed in Chapter 5.

Chapter 3

Determination of the Refractive Index of Human Tissue Using Low Coherence Interferometry

3.1 Introduction

Knowledge of the refractive index of human tissue is essential for forming a basic understanding of the propagation of light in tissue. Moreover, the refractive index must be known to predict the behavior of light at tissue refractive index interfaces. This structural information is important for medical laser treatment of all kinds, especially the determination of irradiant power dosimetry for laser ablation. Also, measurement of the refractive index of tissue will allow optimization of optical elements for thick section confocal imaging. For example, measurement of the refractive index of tissue would enable proper matching of the objective's immersion fluid to the tissue. Finally, *a priori* knowledge of tissue refractive index is necessary for OCT enhanced confocal microscopy in order to correctly match the reference arm to the focal position.

In many cases, the refractive index of human tissue is of physiological significance. For example, the refractive index of the human stratum corneum is related to tissue hydration states and may be altered during certain diseases such as eczema. In addition, local variation in refractive indices gives rise to contrast in OCT images. The change in the refractive index of lipid in human atherosclerotic plaques versus the surrounding supportive tissue may provide sufficient contrast to diagnose lesions prone to rupture[9].

However, little has been done to quantify the refractive index of tissue. The primary reason for the lack of research in this area is the highly scattering, heterogeneous nature of tissue. Scattering in tissue makes it impossible to measure tissue refractive index by traditional refractive index measurement techniques for transparent specimens such as white light interferometry, prismatic dispersion, and planar reflection methods[10].

3.2 Past Research

The only comprehensive study of tissue refractive index has been performed by measuring the angle of multimode light transmission through a bare optical fiber embedded in tissue[10]. The output angle of transmission of the light from the fiber is related to the index of the core and the surrounding medium or cladding by

$$n_s = \sqrt{n_q^2 - [\sin(\theta)]^2} \qquad (3.2.1)$$

where n_s is the refractive index of the sample and n_0 is the refractive index of the core.

For these experiments, the core of the fiber was immersed in homogenized tissue, serving as the cladding for the fiber. Light was coupled into the fiber and the output from the fiber was measured as a function of angle. Using this arrangement, bovine muscle was found to have a refractive index of 1.41, while bovine adipose tissue was found to have a refractive index of 1.45[10]. The major disadvantage to this technique is that the internal structure of the sample is destroyed by homogenization.

In vivo measurement of the refractive index of transparent tissue has been attempted by Gahm, et. al.[11]. This group used a microscope to focus on the surface of a thin transparent layer. The stage of the sample was then moved up and the microscope was focused on the slide underneath the sample. Since the actual thickness of the sample was known, the optical thickness was calculated using the known stage movement between the two foci and marginal ray analysis. Using this method, the refractive index of rat mesentery was measured to be approximately 1.52[11]. This technique would be impossible to implement in multiply scattering tissue, however, because it must be performed on a transparent specimen of known thickness.

Two methods are presented here to determine the refractive index of human tissue. The first method uses the ability of OCT to the measure optical pathlength of excised tissue specimens. The second method employs OCT enhanced confocal microscopy to track the focal position as the sample is scanned through the focus.

3.3 Optical Pathlength Measurement

The optical pathlength method for measuring the refractive index is applicable to *in vitro* tissue samples. This technique is simple to implement so it may be used for rapid cataloging of the refractive indices of different tissue types. Moreover, as opposed to the techniques proposed by Bolin et. al[10], this method measures the refractive index of intact tissue samples and thus is less invasive than the fiber transmission technique.

3.3.1 Theory

Since the OCT system detects the envelope of the autocorrelation function, the group optical pathlength is measured as opposed to the phase optical pathlength. The group refractive index may be obtained using a Taylor series expansion of the propagation constant, β around the center frequency, ω_0:

$$\beta(\omega) = \beta(\omega_0) + \frac{d\beta(\omega_0)}{d\omega}(\omega - \omega_0) + \frac{d\beta^2(\omega_0)}{d\omega^2}(\omega - \omega_0)^2, \tag{3.3.1}$$

where

$$a_1(t) = A_1(t)\exp[j(\omega_0 t - \beta(\omega)z)] \tag{3.3.2}$$

and $A_1(t)$ is the slowly varying envelope of the incident field.

The propagation constant, $\beta(\omega)$, can be rewritten to first order as:

$$\beta(\omega) = \beta(\omega_0) + \frac{1}{v_g}(\omega - \omega_0) \tag{3.3.3}$$

where v_g is the group velocity. The group velocity may also be defined in terms of c, the speed of light in free space, and n_g, the group refractive index:

$$v_g = \frac{c}{n_g}. \tag{3.3.4}$$

Also, since

$$\beta = \frac{\omega_0}{c} n, \tag{3.3.5}$$

$$\frac{1}{v_g} = \frac{d\beta}{d\omega_0} = \frac{n}{c} + \frac{\omega_0}{c}\frac{dn}{d\omega_0}. \tag{3.3.6}$$

Finally, using Equations 3.3.4 and 3.3.6,

$$n_g = n + \omega_0 \frac{dn}{d\omega_0}. \tag{3.3.7}$$

Equation 3.3.7 states that the group index is a function of the derivative of the phase index with respect to the center frequency, ω_0. Because the phase refractive index does not vary appreciably with ω_0 for tissue, the group refractive index can be considered equal to the phase refractive index.

The use of OCT to measure the optical pathlength of a sample can be understood by analyzing the scattering two-port of a Michelson interferometer with a sample of index n_s in the sample arm (Figure 3.1).

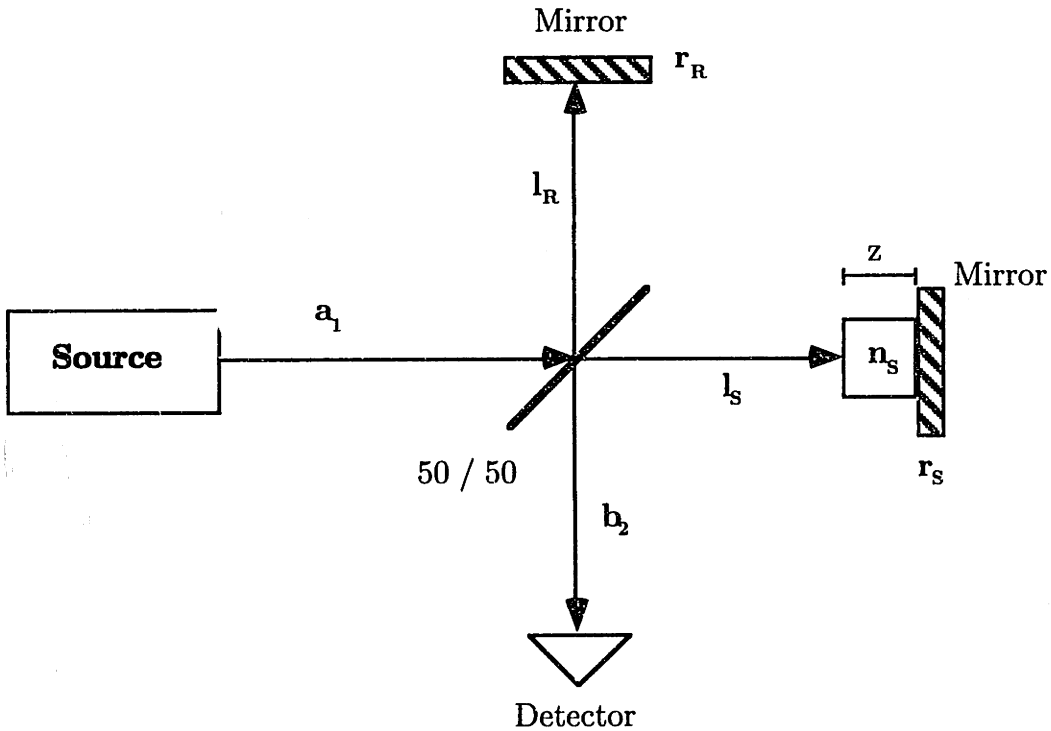

Figure 3.1. Schematic of Michelson interferometer with index mismatch in sample arm.

For coherent incident light, the scattering matrix analysis of the interferometer for $r_1 = r_2 = 1$ shows that

$$\frac{\langle |b_2| \rangle^2}{\langle |a_1| \rangle^2} = \cos^2\left[k(l_r - l_s + z(1 - n_s))\right]. \tag{3.3.8}$$

If we define

$$\Delta n = (n_s - 1), \tag{3.3.9}$$

then a maximum interferometric signal occurs when $l_r = l_s + z\Delta n$. In free space, for example, $\Delta n = 0$ and maximum interference occurs when the arms are pathlength matched.

The refractive index of a tissue sample can be determined by placing the tissue on top of a reflecting surface and measuring z from the OCT image. Specifically, z can be determined by measuring the distance from the surface to the location where the reflector would be in the OCT image if the index of the sample medium were one, z_0 (Figure 3.4). Therefore,

$$z = z_s - z_0, \tag{3.3.10}$$

where z_s is the axial position of the surface of the sample in the OCT image. We can then determine $z\Delta n$ by measuring the distance from the reflector in the OCT image to z_0 (Figure 3.4). Thus, $z\Delta n$ is defined by:

$$z\Delta n = z_0 - z_r, \tag{3.3.11}$$

where z_r is the axial position of the reflector below the sample in the OCT image. Finally, the refractive index of the sample, n_s, may be determined by using the definition of the optical pathlength:

$$n_s = \frac{z\Delta n + z}{z}. \tag{3.3.12}$$

3.3.2 Methods

System Configuration: The OCT system consists of a single mode fiber optic Michelson interferometer (Figure 2.1). A superluminescent diode with a center wavelength at 1300 nm and a spectral bandwidth of 50 nm was used for the experiments. The system had an axial and transverse resolution of approximately 20 μm, object arm power of 100 μW, and a signal to noise ratio of 110 dB.

Sample Preparation: Samples of different refractive indices were placed on top of a razor blade and imaged using the OCT system. The samples consisted of two types: 1) Phantoms included H_2O (n = 1.33), and microscope immersion oil (n = 1.51) (Figure 3.2). 2) *In vitro* human tissue samples were taken postmortem and consisted of human full thickness skin, diaphragmatic tendon, mesenteric adipose and left ventricular cardiac muscle. All tissue samples were dissected to a thickness of 500 μm and placed on a razor blade (Figure 3.3). The tissue samples were stored in isotonic saline and immersed in sodium azide.

Data Acquisition: OCT images of the samples were acquired by scanning the reference arm to obtain axial reflectance profiles and then moving the sample laterally to create an image. The images were acquired so that the razor blade was viewable at two separate points on the phantom image, so that a line could be drawn through them (Figure 3.4). The images were obtained with spatial dimensions of 2x6 mm. The size of the images were 500x100 pixels. The single image scan time was approximately 10 seconds.

Data Analysis: The centroid of the razor blade was interpolated in the x direction through the sample to find the line $z_0(x)$ (Figure 3.4). Determination of z was accomplished by measuring the distance between the surface and the line $z_0(x)$. The measurement of $z\Delta n$ was accomplished by measuring the distance between the reflectance from the razor blade and the line $z_0(x)$ (Figure 3.4). Data was ratioed to find n_s according to Equation 3.3.12. Five samples were analyzed for each standard and tissue type.

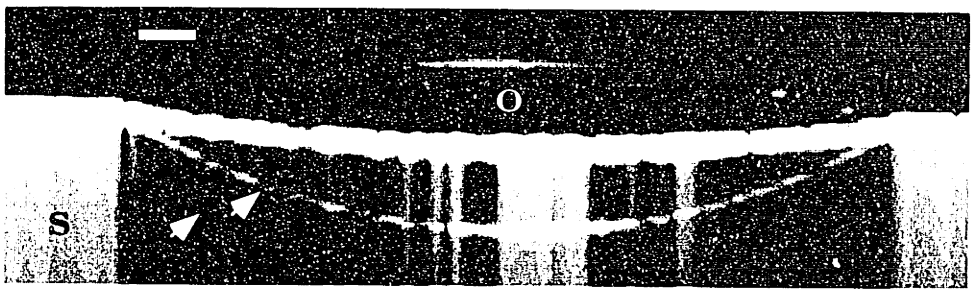

Figure 3.2. OCT image of oil droplet (o) placed on a razor blade. Arrows represent secondary reflections from razor blade. Saturation of the detector (s) occurs in areas of high OCT signal. Image data is plotted as the logarithm of the OCT signal. Bar represents 250 μm.

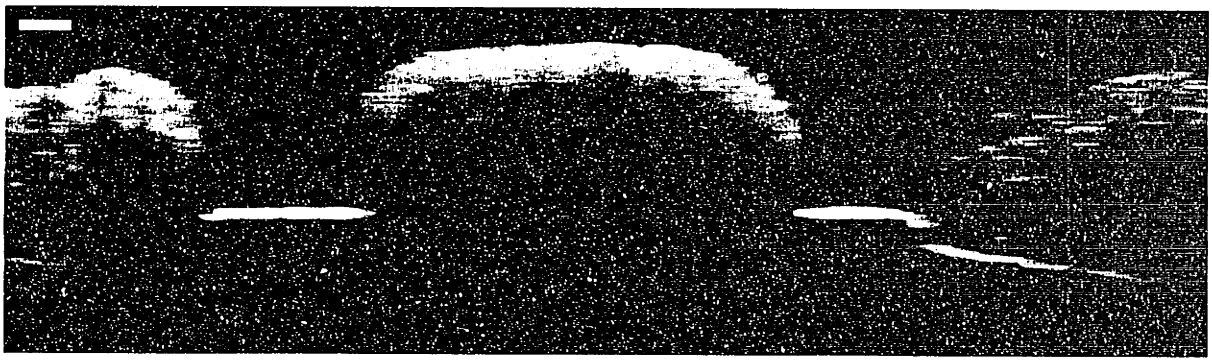

Figure 3.3. OCT image of human diaphragmatic tendon (t), left ventricular cardiac muscle (m), and mesenteric adipose (a), placed on a razor blade. Image data is displayed as the logarithm of the OCT signal. Bar represents 250 μm.

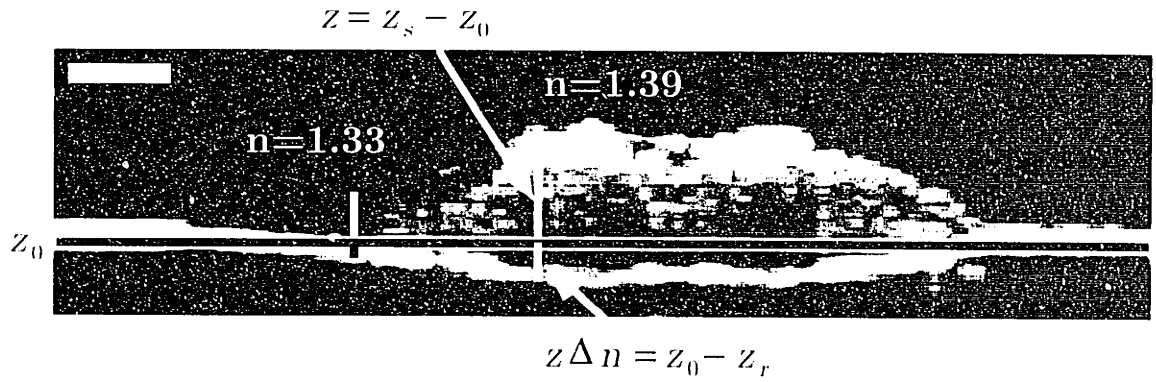

Figure 3.4. OCT image of full thickness human skin placed on a razor blade. Vertical line is reference point for n=1.0. Horizontal bars represent z, $z\Delta n$ from top to bottom. Image data is logarithm of the OCT signal. Upper left hand bar represents 500 μm.

3.3.3 Results

Phantom refractive indices: The phantom images of H_2O (n = 1.33), and microscope immersion oil (n = 1.52) are shown in Figures 3.4, 3.2. The results from the refractive index measurement experiments are shown in Table 3.3.1. These results are compared with known values of the phantom refractive indices obtained from the literature[1].

Substance	Measured n	Known value of n
H_2O	1.33±.012	1.33
Immersion Oil	1.52±.002	1.52

Table 3.3.1 Refractive index measurements for reference phantoms.

Tissue refractive indices: The OCT images of full-thickness human skin, adipose tissue, and muscle are shown in Figure 3.3. The results from the refractive index measurement experiments are shown in Table 3.3.2. These results are compared with estimated values of the corresponding tissue refractive indices obtained from the literature[10,12].

Tissue type	Measured n	Estimated value of n
Skin	1.412±.006	1.40
Muscle	1.39±.001	1.40 (Bovine Tissue)
Adipose	1.48±.007	1.46
Tendon	1.58±.012	Unknown

Table 3.3.2 Refractive index measurements for human tissue specimens.

3.4 Focus Tracking

A change in the refractive index of the sample causes a shift in the focal position as the sample is scanned through the focus. OCT enhanced confocal microscopy may be used to detect this change in focal position The refractive index necessary to produce this focal shift may be then determined using Snell's Law and marginal ray geometric calculations. This method for measuring the refractive index is non-invasive and may be used to measure the refractive index of *in vivo* tissue.

Since *in vitro* tissue may not be an accurate representation of *in vivo* tissue due to tissue degradation and dehydration, measurements of the refractive index using this method are more meaningful than those obtained by *in vitro* methods. Moreover, a non-invasive technique for measuring the refractive index is very powerful because it provides the ability to monitor the composition of *in vivo* tissue. For example, *in vivo* monitoring of the hydrogenation of different tissue types may be used to diagnose and evaluate diseased human tissue.

3.4.1 Theory

The refractive index can be determined using focus tracking because the variation of the refractive index in the axial direction changes the effective focal length. The OCT enhanced confocal microscope may be used to measure the focal shift by first matching the reference arm length to the surface of the sample. When the sample stage is moved a distance, z, into the focus, the focus resides within the medium and the optical pathlength to the focus changes. The reference arm is then moved a distance, Δz, until a maximum interferometric signal is detected. Given z

and Δz, the refractive index can be calculated using Snell's Law and marginal ray geometric calculations.

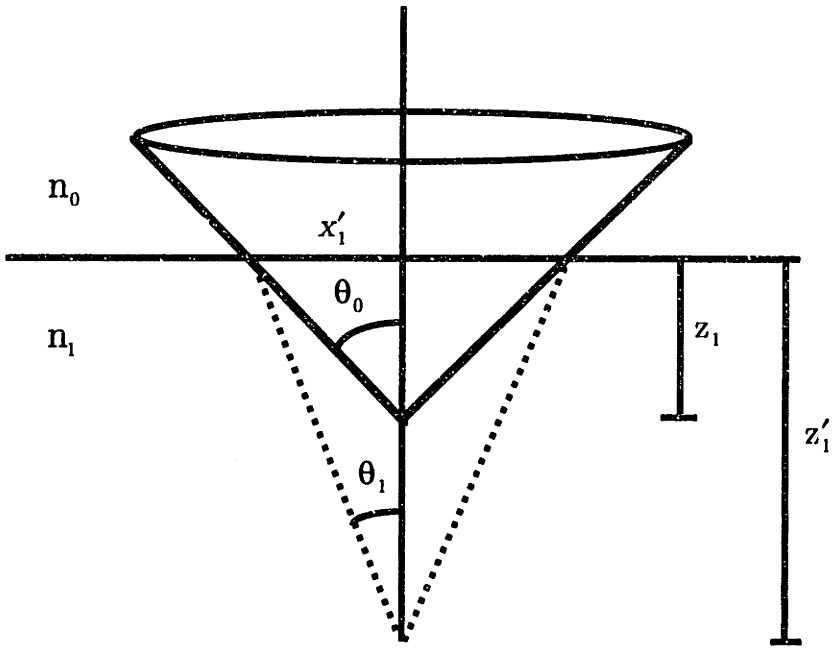

Figure 3.5. Schematic of focus tracking geometry for single index medium.

Figure 3.5 shows a schematic of the focus tracking geometry. For a single index medium, the marginal ray analysis begins with a geometrical determination of the focal shift using Snell's Law:

$$n_0 \sin\theta_0 = n_1 \sin\theta_1 \tag{3.4.1}$$

where

$$\theta_0 = \sin^{-1}\left(\frac{NA}{n_0}\right) \tag{3.4.2}$$

and thus,

$$n_1 \sin\theta_1 - NA = 0\,. \tag{3.4.3}$$

If the reference arm is moved to maximize the interferometric signal from the scattering position within the medium with the refractive index, $n(z)$,

$$\int_0^{z_1'} n(z)dz = n_0 z_1 + n_0 \Delta z_1, \tag{3.4.4}$$

where Δz_1 is the position that the reference arm must be moved for maximum interference, z_1 is the stage travel distance, $n_0 = 1$ for free space, and z_1' is the free space position of the focus in the medium. If the index, $n(z)$ is constant for the integral in Equation 3.4.4, then

$$n_1 z_1' = n_0 z_1 + n_0 \Delta z_1, \tag{3.4.5}$$

and

$$z_1' = \frac{n_0 z_1 + n_0 \Delta z_1}{n_1}. \tag{3.4.6}$$

Using simple geometry from Figure 3.5, it can be seen that:

$$x_1' = z_1 \tan(\theta_0) \tag{3.4.7}$$

and

$$\theta_1 = \tan^{-1}\left(\frac{x_1'}{z_1'}\right) = \tan^{-1}\left[\frac{n_1 z_1 \tan(\theta_0)}{n_0(z_1 + \Delta z_1)}\right]. \tag{3.4.8}$$

Finally, from equation (3.4.3),

$$n_1 \sin\left\{\tan^{-1}\left[\frac{n_1 z_1 \tan(\theta_0)}{n_0(z_1 + \Delta z_1)}\right]\right\} - NA = 0. \tag{3.4.9}$$

The refractive index of the medium, n_1, can be found by finding the root of Equation 3.4.9.

For a many layered medium, the refractive index for each layer can be found by iterating the above theory for each layer, starting at the top layer. Figure 3.6 shows a schematic of the geometry for a two layer medium.

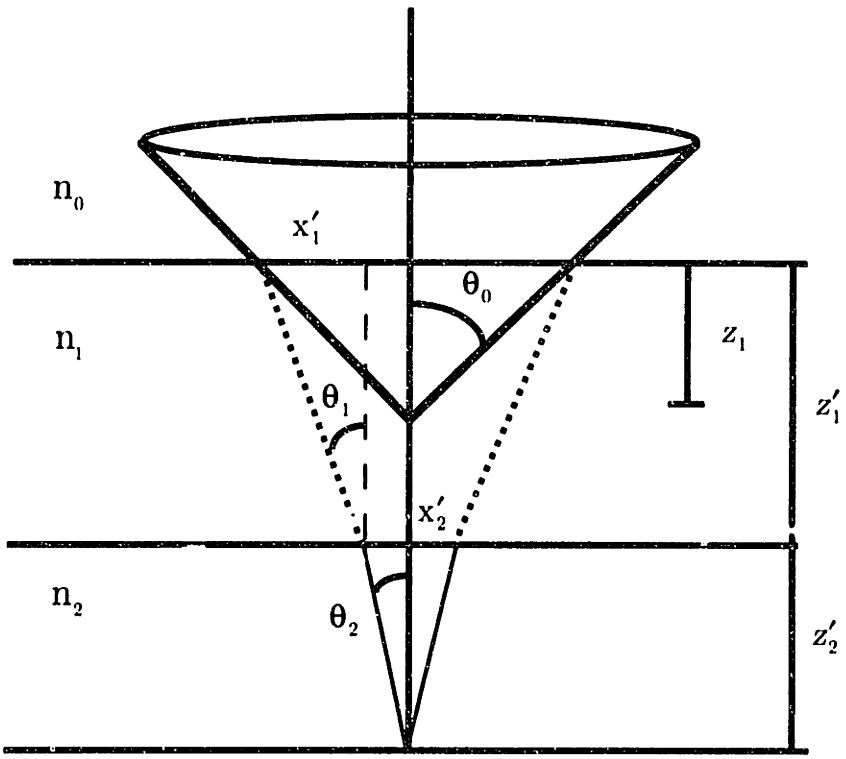

Figure 3.6. Schematic of focus tracking geometry for two-layered index medium.

If, for every position within the sample, the reference arm is moved to maximize the interference at the focus, the following values are known for every layer $0..n$: $\Delta z_{0...n}$, the reference arm maximum interference position for every stage position, $z_{0...n}$, and $n_{0...n-1}$, the calculated refractive index for every previous layer. From each $n_{0...n-1}$, $z'_{0...n-1}$ and $\theta_{0...n-1}$ can be calculated for each previous layer.

Snell's Law still holds:

$$n_n \sin\theta_n - NA = 0 \ , \tag{3.4.10}$$

$$\sum_{k=0}^{n-1} n_k (z'_k - z'_{k-1}) + n_n (z'_n - z'_{n-1}) = \Delta z_n , \tag{3.4.11}$$

and

$$(z'_n - z'_{n-1}) = \frac{1}{n_n}\left[\Delta z_n - \sum_{k=0}^{n-1} n_k (z'_k - z'_{k-1})\right]. \tag{3.4.12}$$

Again, using geometrical relationships from Figure 3.6,

$$x_0' = x_n \tan(\theta_0), \tag{3.4.13}$$

$$x_n' = x_{n-1}' - (z_{n-1}' - z_{n-2}')\tan(\theta_{n-1}) \tag{3.4.14}$$

and

$$\theta_n = \tan^{-1}\left[\frac{x_n'}{(z_n' - z_{n-1}')}\right]. \tag{3.4.15}$$

Finaliy, as before, using Equation 3.4.15 and Snell's Law:

$$n_n \sin\left\{\tan^{-1}\left[\frac{n_n x_n'}{\Delta z_n - \sum_{k=0}^{n-1} n_k (z_k' - z_{k-1}')}\right]\right\} - NA = 0, \tag{3.4.16}$$

and the refractive index for the n^{th} layer may be determined by finding the root of Equation 3.4.16.

This method can be applied iteratively to determine the axial refractive index profiles for the turbid medium if the following assumptions hold: 1) there is scattering at every point; 2) there are no abrupt scattering or absorbing discontinuities in the medium; 3) the medium is composed of layers of homogeneous refractive index. To first order, all of these assumptions hold in human tissue, and when they do not hold, the invalid points can be detected and eliminated from the data.

3.4.2 Methods

System Configuration: The source for the OCT enhanced confocal system was a superluminescent diode with a center wavelength at 850 nm and a spectral bandwidth of 25 nm. The imaging objective was a 40x, 0.95 NA, air immersion objective, giving a transverse resolution of 1 μm. In addition, because the system operated with a high numerical aperture objective, the axial resolution was approximately 1 μm. The object arm had a power of 100 μW, and the detection

signal to noise ratio was 110 dB. Since the reference arm was held fixed for data acquisition at each point, the detection was not accomplished by demodulating the interference signal at the Doppler frequency of the reference arm. Instead, the reference arm was modulated using a piezoelectric transducer at 20KHz and the interference signal magnitude was taken from lock-in detection at the modulation frequency. The reference arm was also supermodulated at a low frequency to reduce quadrature fluctuations [6].

Sample Preparation: A phantom was constructed to measure the refractive index of H_2O. The phantom consisted of a coverslip placed over a drop of H_2O on a mirror (Figure 3.7). The tissue sample was *in vitro* full-thickness human skin. The skin was stored in isotonic saline and immersed in sodium azide. For the experiment, the tissue was dissected to a thickness of 500 μm, and placed on the stage. The skin was imaged with 100% hydration at 25°C.

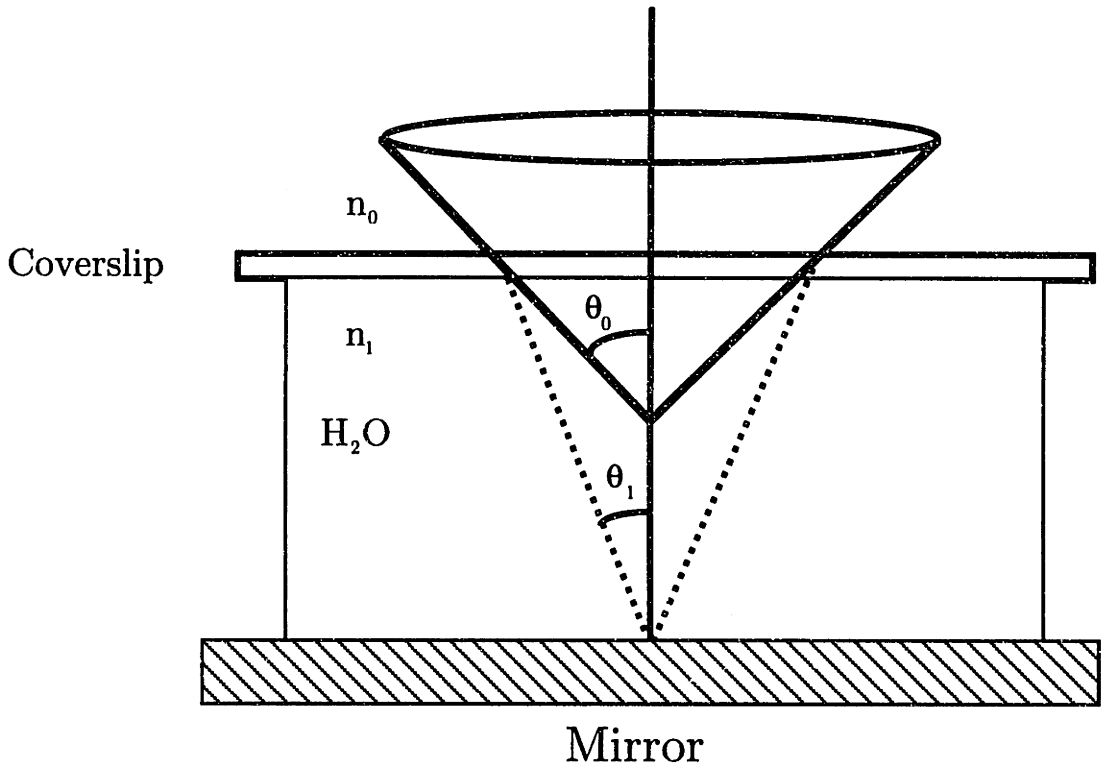

Figure 3.7. Schematic of phantom for determining refractive index using focus tracking.

Data Acquisition: Determination of the refractive index of the H_2O phantom was accomplished by first positioning the focus of the sample arm at the coverslip-H_2O interface. The reference arm was positioned to maximize the interference at the surface. The stage was then moved z_1 until the mirror was at the focus. The reference arm was subsequently repositioned Δz_1 until a maximum interferometric signal was obtained. Using z_1 and Δz_1, the index, n_1, was obtained using Equation 3.4.9.

The tissue refractive index data was obtained by first positioning the focus of the sample arm of the OCT enhanced confocal microscope at the coverslip-tissue interface. Axial scans of the tissue samples were acquired by moving the sample stage z_n into the focus. The reference arm was then moved back and the scan was repeated. This procedure was repeated for 50 different positions of the reference arm, each position lengthened by 2 μm. For each point, the position of the reference arm where the maximum interference occurred, Δz_n, was recorded. The maximum signal was also recorded. The length of each axial scan was 200 μm with a total of 200 pixels per axial scan. The axial profile scan time for each reference arm position was approximately 2 seconds.

Data Analysis: The data was processed to eliminate data points that invalidated the assumptions of Section 3.4.1. Overestimation of the position of the maximum interference occurred when a strong reflector was deeper than the current point. Underestimation of the position of maximum interference occurred when a strong reflector was above the current point. All reflecting points that violated the assumptions of Section 3.4.1 were eliminated from the final data. To accomplish this, only reference arm positions at the local maxima of the maximum OCT signal were used in the data analysis. Once the over and underestimated points were eliminated from the data, the data was segmented into two layers and fit using linear regression. The two layers represented the stratum corneum, n_1 and the epidermis, n_2.

3.4.3 Results

Phantom refractive indices: The refractive index of the H_2O (n = 1.33) phantom was determined to be 1.33 ± 0.009 using Equation 3.4.9.

Tissue refractive indices: The raw data from the axial scans of full-thickness skin is shown in Figure 3.8. The processed interpolated data is shown in Figure 3.9. The results from the focus tracking experiment are shown in Table 3.4.1 and compared with the estimated values of skin refractive indices obtained from the literature[12].

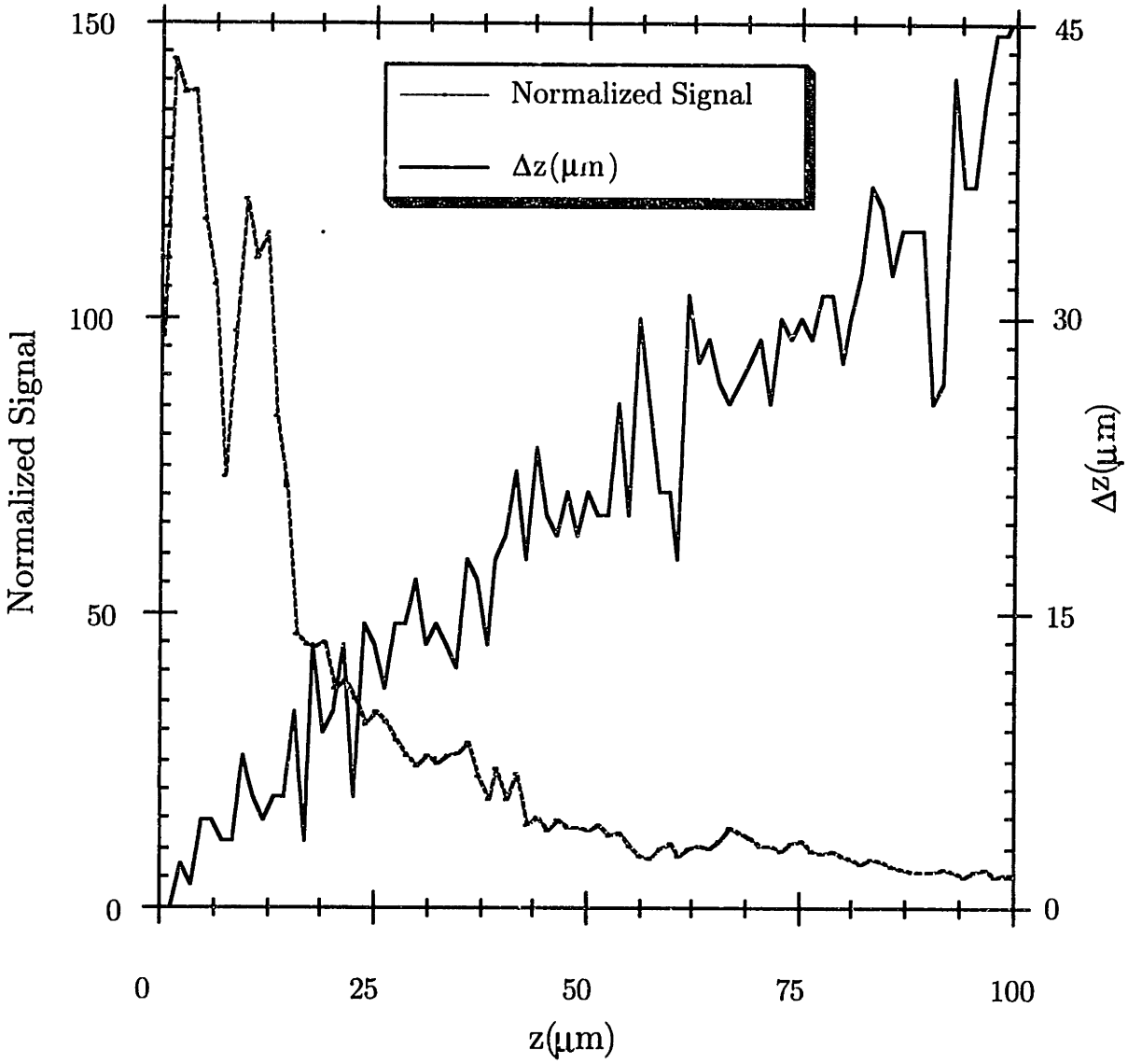

Figure 3.8. *In vitro* human skin. Raw data from focus tracking experiment.

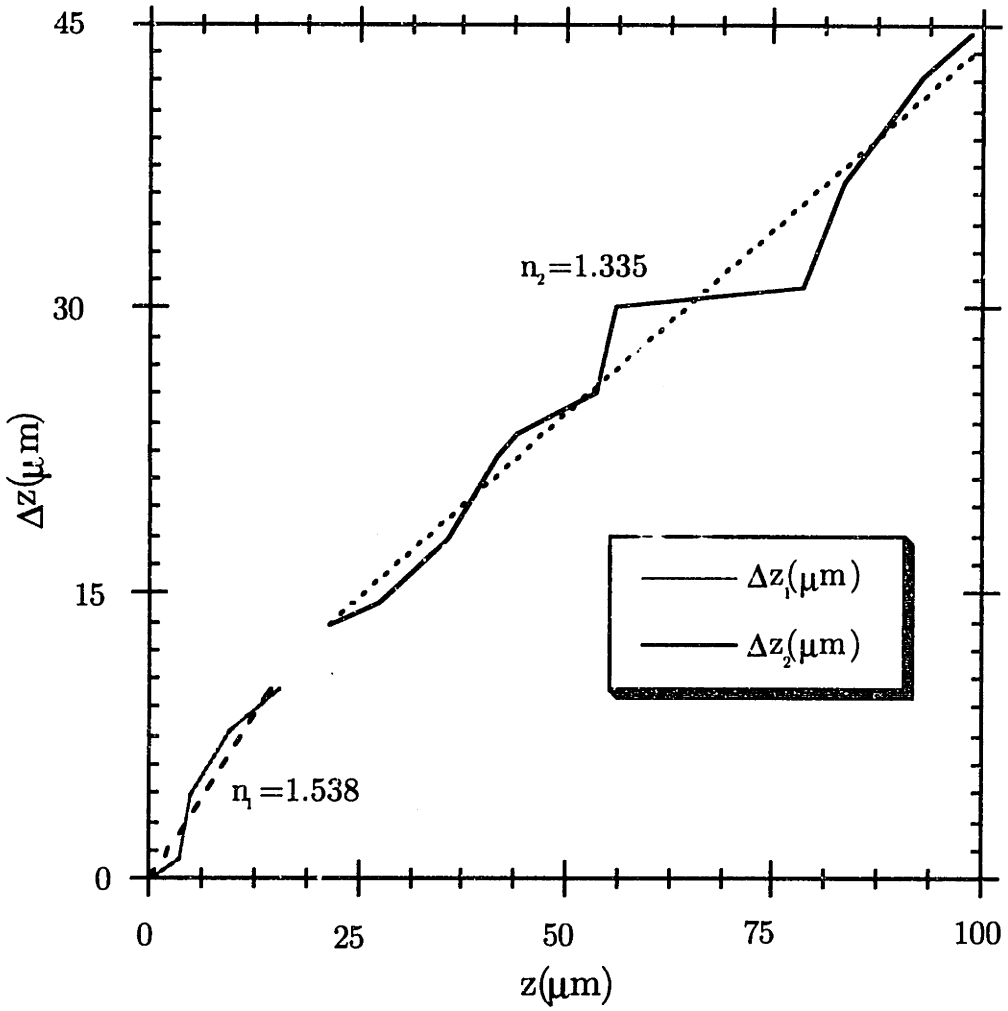

Figure 3.9. *In vitro* human skin. Processed data from focus tracking experiment.

Tissue type	Measured n	Estimated value of n
Stratum Corneum	1.538	1.55
Epidermis	1.335	1.34

Table 3.4.1 Results of refractive index measurements for human tissue specimens.

3.4.4 Discussion

The measurement of the refractive indices using the optical pathlength measurement by OCT is shown to be an effective method for measuring the bulk refractive index for different tissue types. Although this method is invasive, it is very simple and does not rely on tissue homogenization for reliable results.

The measurement of the refractive index by focus tracking provides results that are consistent with predicted values for *in vivo* human tissue. Because focus tracking is non-invasive, it should become a promising new technique for measurement of the refractive index of *in vivo* human tissue. This tool will enable a further understanding of the physiological constituents of human tissue during normal physiological and pathological processes. Moreover, measurement of the refractive indices using either method will aid in determining contrast mechanisms for OCT cross-sectional imaging.

Chapter 4

Determination of the Optical Properties of Human Tissue Using Low Coherence Interferometry

4.1 Introduction

A simple method for quantitatively determining the optical properties of *in vivo* tissue would greatly enhance optical diagnosis and treatment in medicine. Once the optical properties of tissue are known, the three-dimensional transport of light through the tissue can be predicted. Detailed knowledge of the absorption coefficient, μ_a, the scattering coefficient, μ_s, and the anisotropy coefficient, g, in tissue will allow for better planning of laser treatment and surgery. For example, the ability to calculate the absorption coefficient, and thus the concentration of exogenous fluorescent dye in tissue will enable physicians to determine the irradiant dose for tumor destruction during the photodynamic therapy of cancer. In addition, *in vivo* quantification of the concentration of tissue endogenous chromophores is useful as both a clinical and basic science tool. Finally, images of spatial variations in tissue scattering and absorption can provide much insight into underlying disease processes.

4.2 Scattering Theory

Scattering of electromagnetic radiation can be segmented into three regimes: 1) scattering by particles much smaller than the wavelength, or Rayleigh scattering; 2) scattering by particles sized on the order of the incident wavelength, or "Mie Scattering"; 3) scattering by particles much larger than the wavelength, or Thompson Scattering.

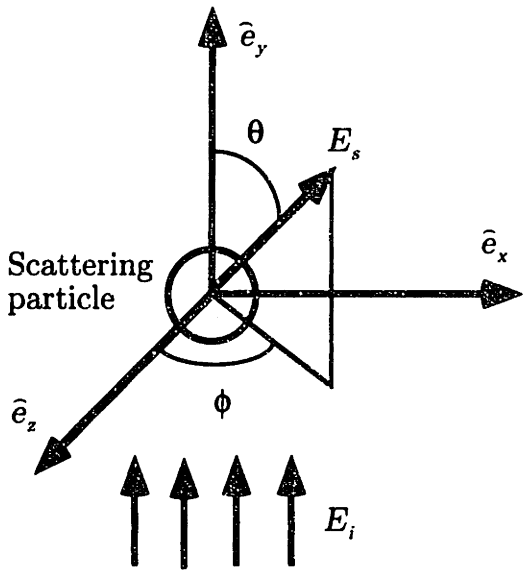

Figure 4.1. Scattering geometry for a spherical particle[13].

The geometry for the scattering by a sphere is shown in Figure 4.1. In the far field or $\mu_s z >> \lambda$, the relationship between scattered and incident electrical fields can be expressed in spherical coordinates in the following form:

$$\begin{bmatrix} E_{\parallel s} \\ E_{\perp s} \end{bmatrix} = \frac{\exp(jk[r-z])}{-jkr} \begin{bmatrix} S_1 & S_3 \\ S_4 & S_2 \end{bmatrix} \begin{bmatrix} E_{\parallel i} \\ E_{\perp i} \end{bmatrix}, \tag{4.2.1}$$

where S is the scattering matrix of the spherical particle and S is dependent on the scattering angle, θ.

The scattering matrix is calculated by Mie theory. Mie theory is a solution for the scattered electrical field of a plane wave incident on a dielectric sphere of arbitrary size. The method for calculating the scattering matrix using Mie theory is outside of the scope of this thesis, but is documented in several publications[13]. Source code for determining the scattering matrix of a spherical particles is presented in Appendix A.

The transmission of light scattered by a particle may be quantified by analyzing the scattering energy rate. Once the scattering matrix for the particle

has been determined, the rate at which energy is scattered across a closed surface, A, surrounding the particle may be defined as:

$$W_{ext} = -\int_A S_{ext} \cdot \hat{e}_r dA, \tag{4.2.2}$$

where

$$W_{ext} = W_s + W_a, \tag{4.2.3}$$

is the sum of the energy absorption rate and the energy scattering rate[13].

The vector scattering amplitude $X(\theta)$, can be defined from the scattering matrix for a given value of ϕ as:

$$X(\theta) = (S_2(\theta)\cos(\phi) + S_3(\theta)\sin(\phi))\hat{e}_{\perp s} + (S_4(\theta)\cos(\phi) + S_1(\theta)\sin(\phi))\hat{e}_{\parallel s}). \tag{4.2.4}$$

After some algebraic manipulation of Equations 4.4.2 and 4.4.4, the total extinction cross section for the particle, C_{ext}, can be defined as:

$$C_{ext} = \frac{4\pi}{k^2}\mathrm{Re}\{(X \cdot \hat{e}_x)_{\theta=0}\}, \tag{4.2.5}$$

where

$$C_{ext} = C_s + C_a. \tag{4.2.6}$$

The scattering particle can now be thought of as an opaque disk with an area of C_{ext}. This disk is perpendicular to the direction of propagation and removes radiation in the forward, or $\theta = 0$ direction[13].

After summing contributions of discrete scattering events in a slab, the transmitted irradiation through a slab of thickness, h, may be defined as:

$$E_t = E_i \exp\left(-\frac{2\pi\eta h}{k^2}(X \cdot \hat{e}_x)_{\theta=0}\right), \tag{4.2.7}$$

or

$$I_t = I_i \exp\left(-\frac{4\pi\eta h}{k^2}(X \cdot \hat{e}_x)_{\theta=0}\right) = I_i \exp(-\mu_t h)\ , \tag{4.2.8}$$

where η is the volume density of the particles in the slab and

$$\mu_t = \eta C_{ext}. \tag{4.2.9}$$

The total attenuation coefficient, μ_t, has units of inverse length. Equation 4.2.8 is the familiar formulation of Beer's Law[13].

For a non-absorbing spherical particle, $S_3 = S_4 = 0$. Thus,

$$S(\theta) = \begin{bmatrix} S_1(\theta) & 0 \\ 0 & S_2(\theta) \end{bmatrix}. \tag{4.2.10}$$

Once the scattering matrix has been calculated, several directional components of the scattered radiation may be computed. The mean cosine of the scattering phase function, g, is defined to be :

$$g = \langle \cos(\theta) \rangle = \frac{1}{C_s} \int_{4\pi} \left[|S_1(\theta)|^2 + |S_2(\theta)|^2 \right] \cos(\theta) d\Omega. \tag{4.2.11}$$

The backscattering coefficient represents the magnitude of the field that is backscattered in the $\theta = \pi$ direction. The radar backscattering cross section is defined as:

$$C_b = 4\pi \frac{|X(\pi)|^2}{k^2} \tag{4.2.12}$$

and

$$\mu_b = \eta C_b. \tag{4.2.13}$$

In general, Raleigh scattering occurs for small particle or molecular scattering in a human tissue. Rayleigh scattering gives rise to isotropic, or $g = 0$ scattering and a high radar backscattering coefficient. In tissue, "Mie Scattering" or scattering on the order of the wavelength, dominates[12]. Typical values for g in human tissue range from $g \Rightarrow 0.6 - 0.99$[14]. In addition, the radar backscattering coefficient, μ_b, decreases as the value of g increases and thus less light is backscattered from the particle. Thompson scattering is much less commonly seen in tissue and represents the reflectance from large refractive index interfaces.

4.3 Radiative Transport Theory

To understand the propagation of light in tissue, a model for the transport of light must be used to predict the radiative fluence that eventually forms the reflected signal. The transport of photons in an anisotropic scattering media has been modeled by Boltzmann transport theory[15]. The Boltzmann equation for remittance is:

$$\nabla\Phi(r,\Omega)+\mu_t\Phi(r,\Omega)=\int\mu_s p(\theta)\Phi(r,\omega)d\Omega+S(r,\Omega). \tag{4.3.1}$$

The energy fluence rate, Φ, is equal to the radiance integrated over a 4π solid angle normal to the direction vector Ω about position r. The scattering phase function $p(\theta)$ defines the direction of a scattering event. $S(r,\Omega)$ is the volume source term[15]. The optical properties unique to tissue in the Boltzmann equation are μ_a, the absorption coefficient, μ_s, the scattering coefficient and μ_t, the total attenuation coefficient, where

$$\mu_t=\mu_s+\mu_a. \tag{4.3.2}$$

The absorption coefficient is linearly related to the concentration of the absorber, such that

$$\mu_a=\varepsilon[Ab] \tag{4.3.3}$$

where ε is the molar extinction coefficient for the absorber and $[Ab]$ is the concentration of the absorber.

The optical properties of tissue, μ_a, μ_s, and μ_t, can also be expressed in terms of transport mean free paths such that

$$\lambda_a=1/\mu_a, \tag{4.3.4}$$
$$\lambda_s=1/\mu_s, \tag{4.3.5}$$
$$\lambda_t=1/\mu_t, \tag{4.3.6}$$

where λ_a is the absorption mean free path, λ_s is the transport scattering mean free path, and λ_t is the total attenuation mean free path.

Often, the mean cosine of the scattering phase function, g, is combined with μ_s to form the transport scattering coefficient:

$$\mu_s' = \mu_s(1-g). \tag{4.3.7}$$

Propagation of light described using the transport scattering coefficient can be considered isotropic since the scattering coefficient has been normalized by the anisotropy coefficient, g.

In general, the Boltzmann transport equation cannot be solved. Thus, the diffusion approximation to the transport equation is often used to analytically model the transport of light in tissue. The diffusion equation for radiative transport is:

$$D\nabla^2\Phi - \mu_a\Phi + S = 0 \tag{4.3.8}$$

where D is the diffusion coefficient defined by:

$$D = \frac{1}{3(\mu_s' + \mu_a)}. \tag{4.3.9}$$

Analytical solutions for the diffusion approximation can be found for limited geometry's in homogeneous media. However, the diffusion theory approximation breaks down near the source, boundaries, and strong absorbers[16].

4.4 Past Research

The most significant methods that have been investigated for determining the optical transport properties of tissue include diffuse reflectance spectrophotometry, time-resolved reflectance spectrophotometry, and low coherence interferometry .

4.4.1 Diffuse Reflectance Spectrophotometry

Diffuse reflectance spectrophotometry uses the diffusion approximation along with spatial reflectance measurements to obtain μ_a and μ_s'[17]. The optical properties may be determined by first measuring the transport albedo,

$$a' = \frac{\mu_s'}{(\mu_s' + \mu_a)}. \tag{4.4.1}$$

The transport albedo can be calculated from the total diffuse reflectance, R, by solving the diffusion equation subject to boundary conditions that incorporate refractive index mismatches:

$$R = \frac{a'}{1 + 2k(1-a') + 1 + \frac{2k}{3}\sqrt{3(1-a')}} \tag{4.4.2}$$

where

$$k = \frac{1 + r_d}{1 - r_d} \tag{4.4.3}$$

and r_d is empirically related to the refractive index of the media in a known manner[17].

Next, the reflectance is measured as a function of distance from the source entry point in the tissue, ρ. Diffusion theory predicts that at large ρ, the slope of $\ln[\rho^2 R(\rho)]$ vs. ρ approaches $-\mu_{eff}$, where

$$\mu_{eff} = \sqrt{3\mu_a[\mu_a + (1-g)\mu_s]}. \tag{4.4.4}$$

This method has been shown to measure μ_a and μ_s' with approximately 20% accuracy in a homogenous medium[17]. However, at the approximate μ_a and μ_s' of tissue (i.e. μ_a, $= .2$ mm^{-1} and $\mu_s' = 3$ mm^{-1}) the distance, ρ at which the slope of $\ln[\rho^2 R(\rho)]$ converges to $-\mu_{eff}$ is greater than 1 cm. Assumptions of tissue homogeneity over this distance are not realistic. Because of this limitation, diffuse reflectance spectrophotometry can only apply to large homogeneous scattering volumes. The resultant poor resolution precludes the use of this approach. Finally, because the model is based on the diffusion approximation, it is highly inaccurate at scattering boundaries and near the irradiant source entry point.

4.4.2 Time-Resolved Spectrophotometry

Time-resolved spectrophotometry is a technique which measures the reflectance as a function in time after irradiation by a short (picosecond) pulse[18]. Multiple scattering causes the pulse to spread in time. The shape of the remitted pulse is used to determine the optical properties of the medium. The photon fluence rate, $\phi(t)$, from the tissue obeys the time-dependent diffusion equation:

$$\frac{n}{c}\frac{\partial}{\partial t}\phi(\mathbf{r},t) - D\nabla^2\phi(\mathbf{r},t) + \mu_a\phi(\mathbf{r},t) = S(\mathbf{r},t). \tag{4.4.5}$$

For a short pulse from an isotropic point source in an infinite slab medium, the equation can be solved for the reflectance at the surface

$$R(\rho,t) = \left(\frac{4\pi Dc}{n}\right)^{-3/2} \exp\left(-\mu_a \tfrac{c}{n} t\right) \exp\left(-n\left(\frac{(z-z_0)^2+\rho^2}{4Dct}\right)\right) \tag{4.4.6}$$

where

$$\rho = \sqrt{x^2+y^2} \tag{4.4.7}$$

and

$$z_0 = \frac{1}{\mu_s'}. \tag{4.4.8}$$

The absorption coefficient can be obtained by measuring the slope of the logarithm of the reflectance at times much longer than the incident pulse length:

$$\lim_{t\to\infty} \log\left[\frac{\partial}{\partial t} R(\rho,t)\right] = \frac{-\mu_a c}{n}. \tag{4.4.9}$$

The transport scattering coefficient is determined from the time at which the reflectance signal is maximal:

$$\mu_s' = \frac{1}{3\rho^2}\left[4\mu_a\left(\frac{c}{n}\right)^2 t_{max}{}^2 + 10\frac{c}{n}t_{max}\right] - \mu_a. \tag{4.4.10}$$

Time resolved spectrophotometry has been successfully used to measure the optical properties of *in vivo* human tissue for the human calf: $\mu_a = 0.023$ mm^{-1} and $\mu_s' = 0.85$ mm^{-1} at 760 nm[18].

This method has not been used clinically because of the complicated illumination and detection schemes that are necessary for detection of the reflectance as a function of time. For this reason, several investigators have modified this method by measuring phase of the modulated incident light[19]. Using frequency dependent diffusion theory, the absorption coefficient and the transport scattering coefficient can be measured using the phase offset and the change in modulation of the reflected light[19].

Like diffuse reflectance spectrophotometry, both methods for measuring the optical properties assume tissue homogeneity over a large volume of the media. In addition, since time and phase methods are based on the diffusion approximation, they also break down at boundaries of changing optical properties and near the irradiant source entry point.

4.4.3 Low Coherence Interferometry Methods

Within a limited imaging depth, low-coherence interferometry measures single scattered remittance from tissue. Thus, methods for measuring the optical properties of turbid media using low coherence interferometry assume tissue homogeneity only in the axial direction. As a result, diffusion theory is not necessary for measuring the optical properties using low coherence interferometry. The optical properties can be determined from a more robust solution of the Fresnel Integral and Beer's Law.

The optical properties of *in vitro* and *in vivo* human tissue have been measured by Schmitt, et. al. using low coherence interferometry[20]. In this study, a fiber based low coherence interferometer operating at 1300 nm was applied directly to the sample and the reflectance as a function of depth in the tissue was measured.

This method assumed that the observed reflectance was in the single scattering limit. This assumption holds when $\mu_t z << 1$. The backscattered power as a function of depth can then be expressed as follows:

$$P(z) = P_0 \int_0^d (1-R)A(h')\mu_b \exp(-2\mu_t h')\left|\gamma(z-h'/c)\right| + R\left|\gamma(h'/c)\right| dh \qquad (4.4.11)$$

where R is the Fresnel reflection at the surface due to the fiber/sample refractive index mismatch, P_0 is the incident power, γ is the autocorrelation function of the source, h is the reference arm distance and $h' = n_s h$, where n_s is the refractive index of the sample[20]. The function, A, accounts for the divergence of the beam from the fiber, and at small fiber NA:

$$A = \left(\frac{r_s/2}{r_s/2 + h\theta_h} \right)^2, \tag{4.4.13}$$

where r_s is the radius of the fiber core and θ_h is the half angle of the light emitted from the fiber in the sample medium. Since

$$L_c = \int_0^\infty \left|\gamma(\tau)\right|^2 d\tau << \frac{1}{\mu_t}, \tag{4.4.14}$$

$$\frac{P(z)}{P_0} = \frac{L_c}{2} \mu_b A(z) \exp(-2\mu_t z) \tag{4.4.15}$$

for $R = 0$.

The radar backscattering coefficient, μ_b can be obtained by measuring the detector power $P(z = 0)$:

$$P(0) = P_0 \frac{L_c}{2} \mu_b, \tag{4.4.16}$$

and μ_t can be obtained by exponentially fitting *P(z)/A(z)*[20].

Experiments were performed on bovine tissue using this method. The radar backscattering coefficient, μ_b, of *in vivo* human dermis was determined to be approximately 1.4 mm^{-1} and μ_s, 4.2 mm^{-1}[20].

The primary difficulty with this method is that the single scattering limit requires $\mu_t z << 1$. This limit only allows the optical properties to be measured up to a small depth (100 - 200 μm in human tissue)[20]. Moreover, this technique requires contact with the medium, and thus is limited in its applicability.

4.5 Measurement of the Optical Properties of Human Tissue

The previous method for measuring the optical properties of tissue using low coherence interferometry does not include the sample focusing geometry that is commonly found in OCT imaging systems. Single backscattering theory describes the heterodyne detector current produced by OCT imaging of a scattering medium. This theory allows for the computation of the total attenuation coefficient and the radar backscattering coefficient from OCT axial reflectance profiles.

4.5.1 Theory

Single backscattering theory is an analytical solution for the detector current given a heterodyne detection scheme and the focusing geometry shown in Figure 4.2. The amplitude of the incident beam of the sample arm at the scattering media is computed using the Fresnel Integral through the imaging lens. A spherical particle in the medium then backscatters the incoming wavefunction and this scattered wavefunction is projected back through the imaging system. The sample backscattered reflectance is combined with the local oscillator signal from the reference arm to produce the detector current. The two assumptions of single backscattering theory are: 1) multiply scattered light does not reach the detector; 2) the particle separation is much greater than the wavelength[21].

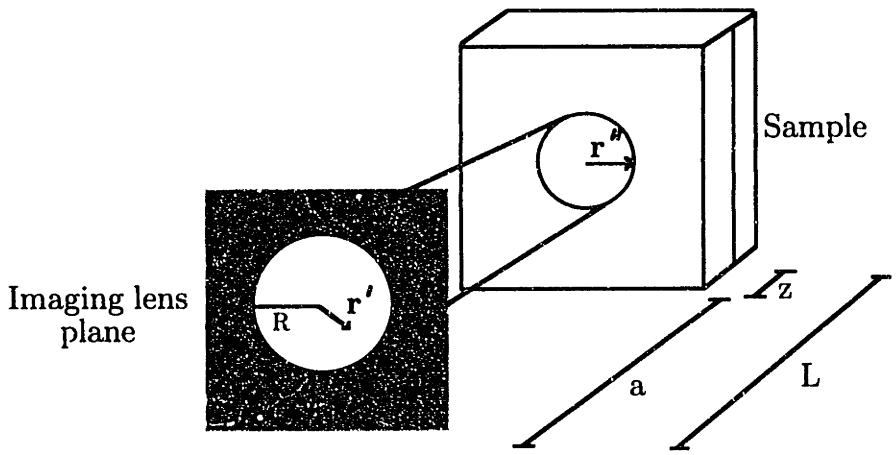

Figure 4.2. Geometry for single backscattering theory[21].

Scattered wavefunction: Using the Fresnel diffraction integral, the wavefunction through the imaging objective at the sample can be written as:

$$\Psi(x,y,L)=\sqrt{\frac{2n_t}{\pi lR\lambda}}\int\exp\left[j\frac{\pi}{\lambda L}(\mathbf{r}-\mathbf{r}'')^2-\frac{j\pi\mathbf{r}''^2}{\lambda \mathrm{f}}-\left(\frac{\mathbf{r}''}{\mathrm{R}}\right)^2\right]dx''dy'', \qquad (4.5.1)$$

where n_t is the number of photons transferred per second. This equation can be integrated by completing the square to give[21]:

$$\Psi(x,y,L)=\frac{R\sqrt{2n_t\pi}}{\lambda L\left[1-\frac{j\pi R^2}{\lambda L}\left(1-\frac{L}{f}\right)\right]}\exp\left(-\frac{\left(\frac{\pi R\mathbf{r}}{\lambda L}\right)^2}{\left[1+\left[\frac{j\pi R^2}{\lambda L}\right]^2\left(1-\frac{L}{f}\right)^2\right]}-j\phi\right), \qquad (4.5.2)$$

where f is the focal length of the lens and ϕ is the phase offset.

Equation 4.5.2 gives the wavefunction at the point x, y, L. At this point, a single particle scatters the wavefunction according to Equation 4.2.1. Since this theory is formulated for spherical particles,

$$S_3(\theta)=S_4(\theta)=0 \qquad (4.5.3)$$

and

$$S_1(\pi)=S_2(\pi) \qquad (4.5.4)$$

Finally, the return wavefunction propagated back through the imaging lens becomes[21]:

$$\Psi_s=\frac{S(\pi)\Psi}{L}\exp\left(-j\left[\frac{\pi}{\lambda f}\mathbf{r}'^2-\frac{\pi}{\lambda L}(\mathbf{r}-\mathbf{r}')^2-\phi\right]\right). \qquad (4.5.5)$$

Heterodyne Signal: The current at the detector with quantum efficiency, η, and a gain, G, is determined by the superposition of the sample wave function and the local oscillator wavefunction[21]:

$$i_s = 2\eta Ge \int_A \Psi_S \Psi^*_{REF} d\mathbf{r}' \tag{4.5.6}$$

where A is the collection aperture and Ψ_{REF} is the reference wavefunction:

$$\Psi_{REF} = \sqrt{\frac{n_{REF}}{\pi R}} \exp\left(-j\phi + \left(\frac{\mathbf{r}'}{R} \right)^2 \right). \tag{4.5.7}$$

When Ψ_{REF} and Ψ_S are substituted into Equation 4.5.6, the mean squared current from the heterodyne signal becomes:

$$\left\langle i_s^2 \right\rangle = \pi n_T n_{REF} R^2 \mu_b \eta^2 G^2 e^2 \int_0^\infty \frac{dL}{L^2 \left[1 + \left[\frac{j\pi R^2}{\lambda L} \right]^2 \left(1 - \frac{L}{f} \right)^2 \right]}, \tag{4.5.8}$$

where the sample beam has been integrated over the spot radius, r'', for a uniform density of particles[21]. The reflectance from the sample derived from the mean squared heterodyne current may be written as:

$$R_s(z) = \frac{\left\langle i_s^2(z) \right\rangle}{i_0^2} = \mu_b \int_0^\infty \frac{\pi R^2 dL}{L^2 \left[1 + \left[\frac{j\pi R^2}{\lambda L} \right]^2 \left(1 - \frac{L}{f} \right)^2 \right]}. \tag{4.5.9}$$

In this form, the single backscattering model does not account for the exponential attenuation in a scattering medium, the effects of the sample refractive index, or the effects of the finite coherence length of the source.

After these parameters have been included, the single backscattered reflectance becomes[22]:

$$R_s(z) = \mu_b \int_0^\infty \frac{\pi R^2 \exp(-2\mu_t z)}{(f + n_s z)^2 \left[1 + \left[\frac{j\pi R^2}{\lambda (f + n_s z)} \right]^2 \left(1 - \frac{(f + n_s z)}{f} \right)^2 \right]} \left| G(\tau) \right|^2 dL, \tag{4.5.10}$$

where the $e^{-2\mu_t z}$ corresponds to the exponential decay to and from the scattering position z. The term $(f + n_s z)$ accounts for the refractive index change in L due to the sample. Finally, $|G(\tau)|^2$ incorporates the effect of the finite coherence length in the single backscatter model.

Since the integral in Equation 4.5.10 yields large values only when the reference and sample arm lengths are matched, the reflectance becomes[22]:

$$R_s(z) = \frac{\pi R^2 L_c \mu_b \exp(-2\mu_t z)}{(f + n_s z)^2 \left[1 + \left[\frac{j\pi R^2}{\lambda(f + n_s z)}\right]^2 \left(1 - \frac{(f + n_s z)}{f}\right)^2\right]}, \tag{4.5.11}$$

with L_c, the coherence length defined as:

$$L_c = \int_{-\infty}^{\infty} |G(\tau)|^2 d\tau. \tag{4.5.12}$$

Single backscatter theory can be further extended to include focusing of the imaging objective at an arbitrary position in the sample. Equation 4.5.11 is valid for an imaging lens with a small numerical aperture if we allow[8]:

$$n_s z \Rightarrow a + n_s z \tag{4.5.13}$$

and

$$f \Rightarrow a + n_s^2 (f - a). \tag{4.5.14}$$

Plots of the reflectance as a function of axial position, z, obtained using single backscatter theory, are shown in Figure 4.3.

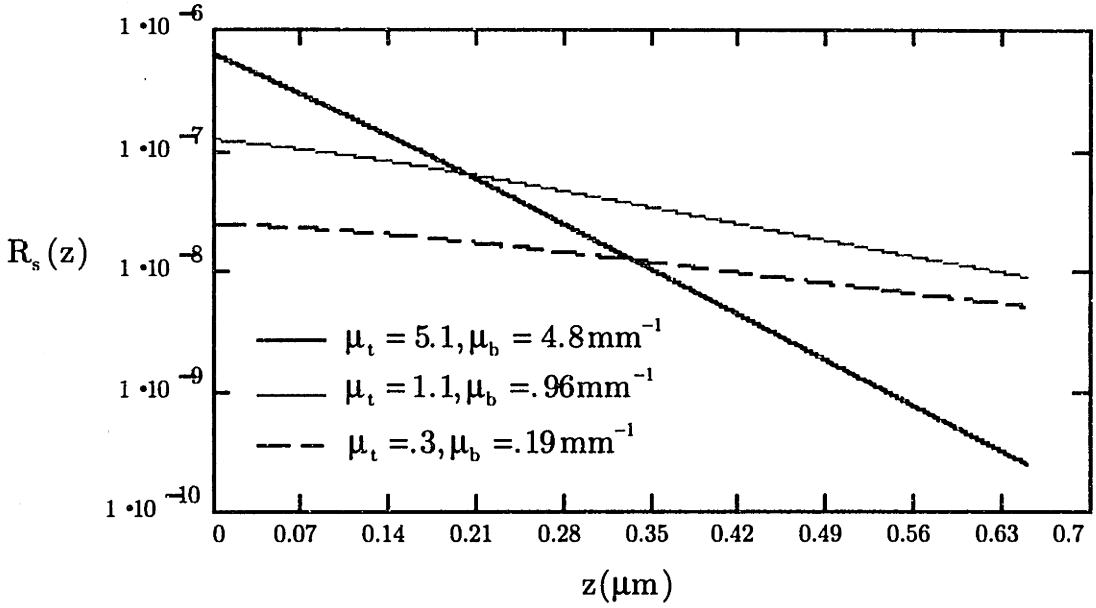

Figure 4.3. Reflectance calculated from single backscatter heterodyne theory for different total attenuation coefficients for 0.3 μm diameter spheres. Sample arm is focused on the surface of the medium. $R = 0.391$ mm, $f = 14.5$ mm, $\lambda = 1.3 \cdot 10^{-3}$mm, $L_c = 0.02$ mm.

Clearly, within the single scattering limit, the optical properties of a turbid medium may be obtained from OCT signal and Equation 4.5.11. The radar backscattering coefficient may be obtained from the OCT signal at the surface, for at z = 0,

$$R_s(z) = \frac{\pi R^2 L_c \mu_b}{f^2}, \tag{4.5.15}$$

and thus,

$$\mu_b = \frac{R_s(z) f^2}{\pi R^2 L_c}. \tag{4.5.16}$$

The total attenuation coefficient may be obtained by logarithmically fitting the axial reflectance profile of OCT signal such that:

$$\mu_t z = -\frac{1}{2}\ln\left[\frac{R_s(z)(f+n_s z)^2\left[1+\left[\frac{j\pi R^2}{\lambda(f+n_s z)}\right]^2\left(1-\frac{(f+n_s z)}{f}\right)^2\right]}{\pi R^2 L_c \mu_b}\right]. \qquad (4.5.17)$$

4.5.2 Methods

System Configuration: The OCT system consists of a single mode fiber optic Michelson interferometer (Figure 2.1). A superluminescent diode with a center wavelength at 1300 nm and a spectral bandwidth of 50 nm was used for the experiments. The system used a 5x objective, resulting in an axial resolution of 30 μm and a transverse resolution of approximately 20 μm. The object arm power was 100 μW, and the signal to noise ratio was 110 dB.

Sample Preparation: Phantoms were constructed using solutions of latex polystyrene microspheres in distilled H_2O. Phantoms with the optical properties at 1300 nm ranging from a μ_t of 0.2 - 5 mm^{-1} were prepared for spheres of 0.3 and 0.966 μm diameter. The optical properties of the phantoms were calculated using Mie theory [Appendix A]. Tissue samples were taken postmortem and consisted of human full thickness skin, mesenteric adipose, and left ventricular cardiac muscle. All *in vitro* tissue samples were dissected to a thickness of 1500 μm and immersed in isotonic saline and sodium azide. The *in vitro* tissues were imaged at 100% hydration at 25°C. Axial OCT reflectance profiles were obtained from *in vivo* human skin. These scans were acquired from the dorsal surface of the index finger of the hand.

Data Acquisition: The beam diameter was measured by scanning a razor blade and using the edge clipping technique[23]. The focal length was determined by measuring the beam diameter and the confocal parameter, b:

$$f = \frac{D}{2}\sqrt{\frac{b\pi}{\lambda}}. \qquad (4.5.18)$$

The reflectance, R_0, was measured from an OCT scan of a mirror. For all of the OCT scans, the sample arm was focused on the surface of the samples, $a = f$. OCT scans of the samples were then acquired by scanning the reference arm to obtain axial reflectance profiles. The axial extent of the scans was 3 mm. The size of the scans was 500 pixels. All scans were averaged 100 times. The total scan time was approximately 200 seconds.

Data Analysis: The data from the OCT scans were normalized by R_0. Background noise was subtracted from all scans. Fresnel reflection was removed for all scans and the $z = 0$ data point was estimated by extrapolating a logarithmic fit of the data for $z > 0$. The radar backscattering coefficient was determined by using the extrapolated $z = 0$ reflectance and Equation 4.5.16. The total attenuation coefficient was calculated by exponentially fitting the OCT axial reflectance profiles up to approximately 200 μm (Equation 4.5.17). Data was only fit up to 200 μm because this was the greatest depth at which all samples had no noticeable effects of multiple scattering. The refractive indices used in the analysis were taken from the results of Chapter 3. Five samples were analyzed for each standard and tissue type.

The optical properties of *in vivo* full thickness human skin were measured by applying Equations 4.5.16 and 4.5.17. Separate exponential fits were used for the epidermis and the dermis. For the calculation of the radar backscattering coefficient, the data at top of the dermal layer was corrected for the exponential attenuation of the epidermis[20].

4.5.3 Results

Phantom optical properties: Figures 4.4 and 4.5 show the plots of the phantom reflectances. Note the correspondence of Figure 4.4 with Figure 4.2. The peak at the beginning of each scan corresponds to the Fresnel reflection at the surface. Figure 4.5 shows the deviation of linear slope where multiple scattering begins to affect the signal.

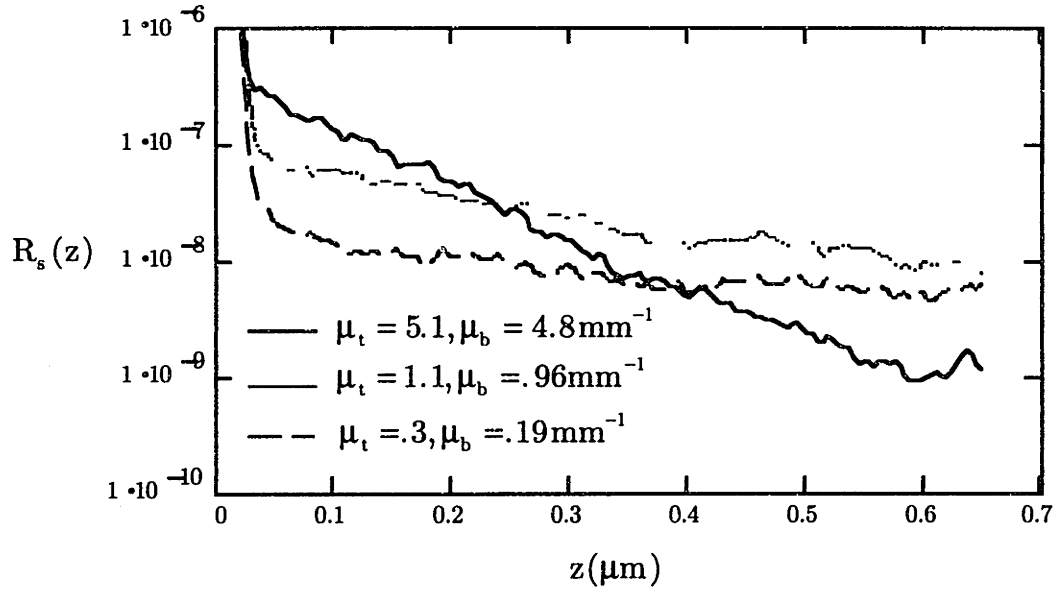

Figure 4.4. Reflectance plots for 0.3 μm diameter latex polystyrene spheres.

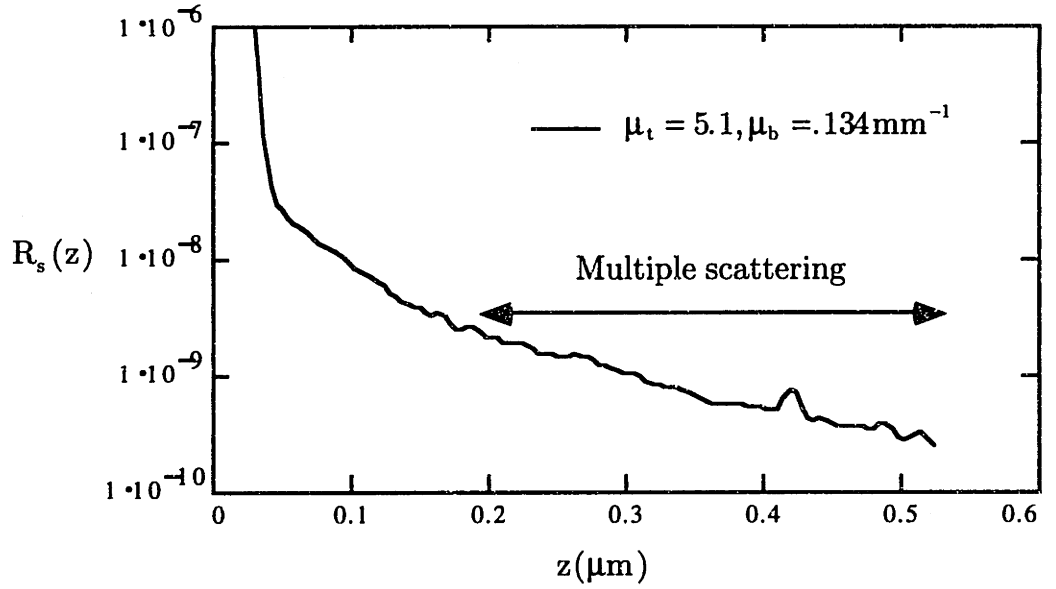

Figure 4.5. Reflectance plot for 0.966 μm diameter latex polystyrene spheres. Multiple scattering begins to effect the exponential decay after approximately 200 μm.

The results of the optical properties measurement of phantoms using single backscatter theory are shown in Table 4.1. These results are compared with known values of the phantom optical properties computed from Mie theory (Appendix A).

Sphere Diameter	Predicted μ_t (mm^{-1})	Measured μ_t (mm^{-1})	Predicted μ_b (mm^{-1})	Measured μ_b (mm^{-1})
0.966	5.1	5.23±.21	0.134	0.135±.014
0.300	5.1	5.12±.06	4.792	4.78±.22
0.300	1.1	1.10±.02	1.062	0.95±.075
0.300	0.3	0.314±.001	0.192	0.2±.004

Table 4.1 Results of optical property measurements for reference phantoms.

Reflectance plots calculated from single backscattering theory are shown in Figures 4.6 - 4.9. The optical properties used in the theoretical fits are taken from Table 4.1. The dotted lines depict theoretical reflectance profiles obtained by varying of the optical properties ±20 percent.

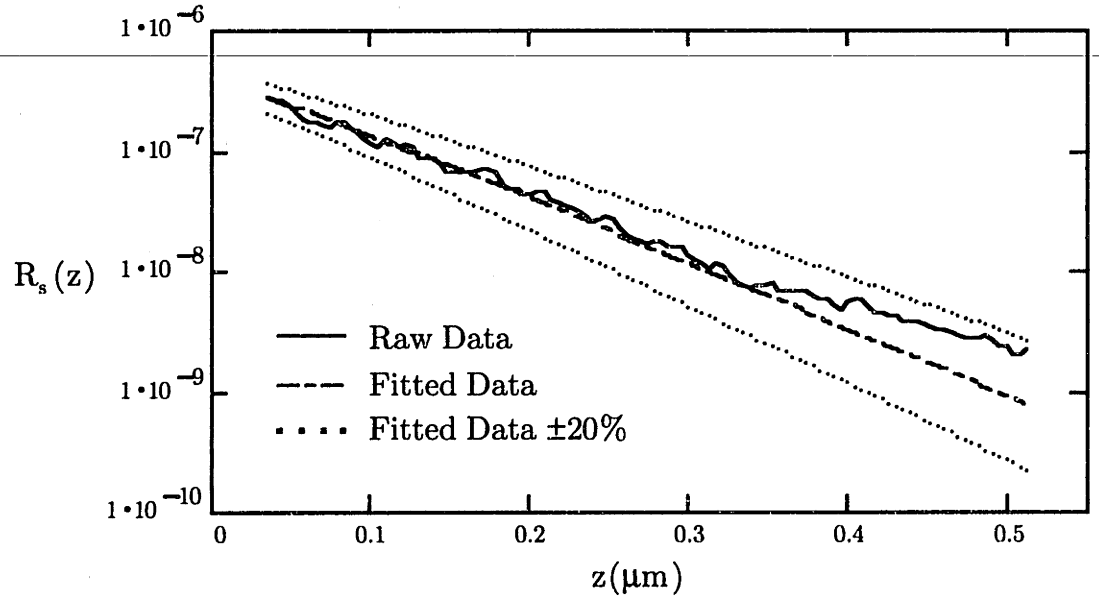

Figure 4.6. Reflectance plot for 0.3 μm diameter latex polystyrene spheres. Fitted data corresponds to reflectance calculated from single backscatter theory using the measured optical properties of the phantom, $\mu_t = 5.23 mm^{-1}$, $\mu_b = 0.134 mm^{-1}$. Dotted lines represent fitted curves for 20% variation from the measured optical properties, $\mu_t = \mu_t \mp 0.2\mu_t$ and $\mu_b = \mu_b \pm 0.2\mu_b$.

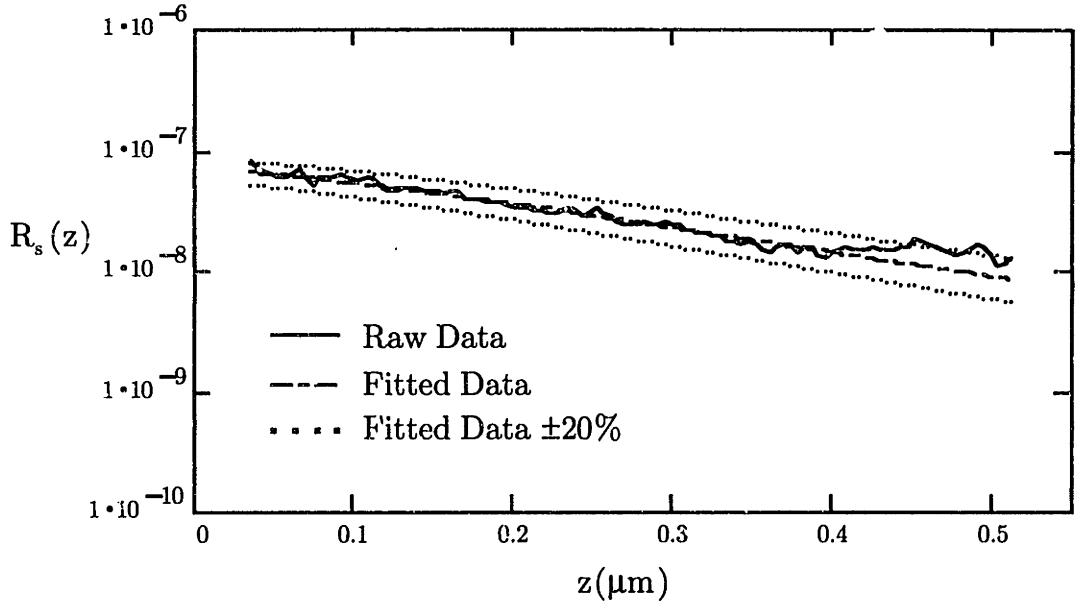

Figure 4.7. Reflectance plot for 0.3 μm diameter latex polystyrene spheres. Fitted data corresponds to reflectance calculated from single backscatter theory using the measured optical properties of the phantom, $\mu_t = 1.1 mm^{-1}$, $\mu_b = 1.06 mm^{-1}$. Dotted lines represent fitted curves for 20% variation from the measured optical properties, $\mu_t = \mu_t \mp 0.2\mu_t$ and $\mu_b = \mu_b \pm 0.2\mu_b$.

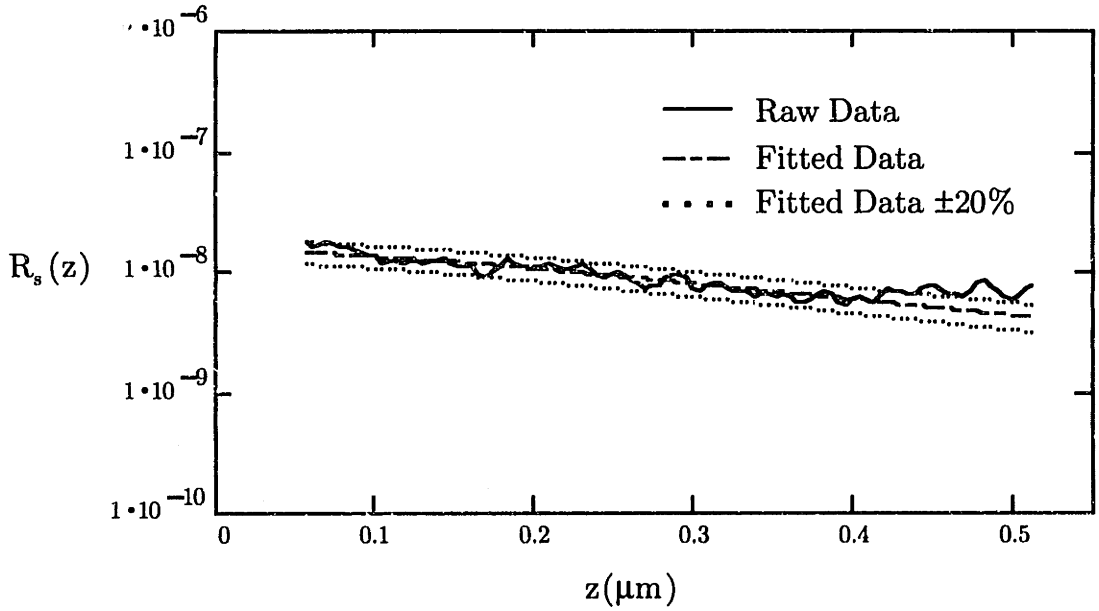

Figure 4.8. Reflectance plot for 0.3 μm diameter latex polystyrene spheres. Fitted data corresponds to reflectance calculated from single backscatter theory using the measured optical properties of the phantom, $\mu_t = 0.32 mm^{-1}$, $\mu_b = 0.19 mm^{-1}$. Dotted lines represent fitted curves for 20% variation from the measured optical properties, $\mu_t = \mu_t \mp 0.2\mu_t$ and $\mu_b = \mu_b \pm 0.2\mu_b$.

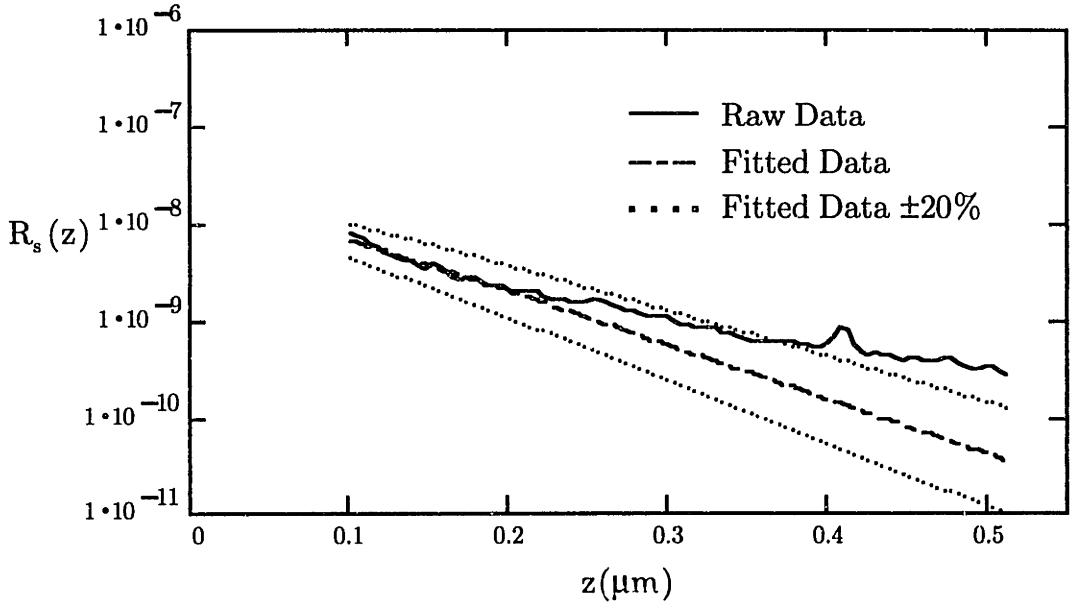

Figure 4.9. Reflectance plot for 0.966 μm diameter latex polystyrene spheres. Fitted data corresponds to reflectance calculated from single backscatter theory using the measured optical properties of the phantom, $\mu_t = 5.23 mm^{-1}$, $\mu_b = 0.134 mm^{-1}$. Dotted lines represent fitted curves for 20% variation from the measured optical properties, $\mu_t = \mu_t \mp 0.2\mu_t$ and $\mu_b = \mu_b \pm 0.2\mu_b$.

In vitro tissue optical properties: Plots of the axial reflectance profiles for muscle, adipose, and skin are shown in Figures 4.10-4.12. The muscle has a much higher negative slope than the adipose tissue. Moreover, the adipose tissue has a very heterogeneous structure, giving rise to the large variation in the OCT signal. Two separate slopes for the reflectance can be seen in the OCT scan of the skin. These two layers probably correspond to the epidermis and dermis, respectively.

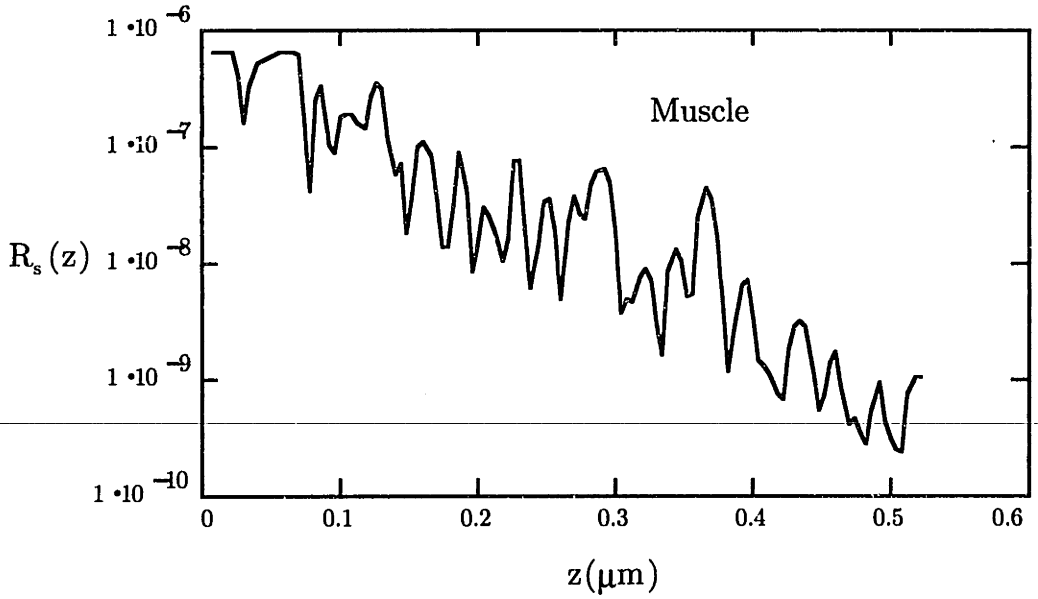

Figure 4.10. Reflectance plots for *in vitro* left ventricular muscle.

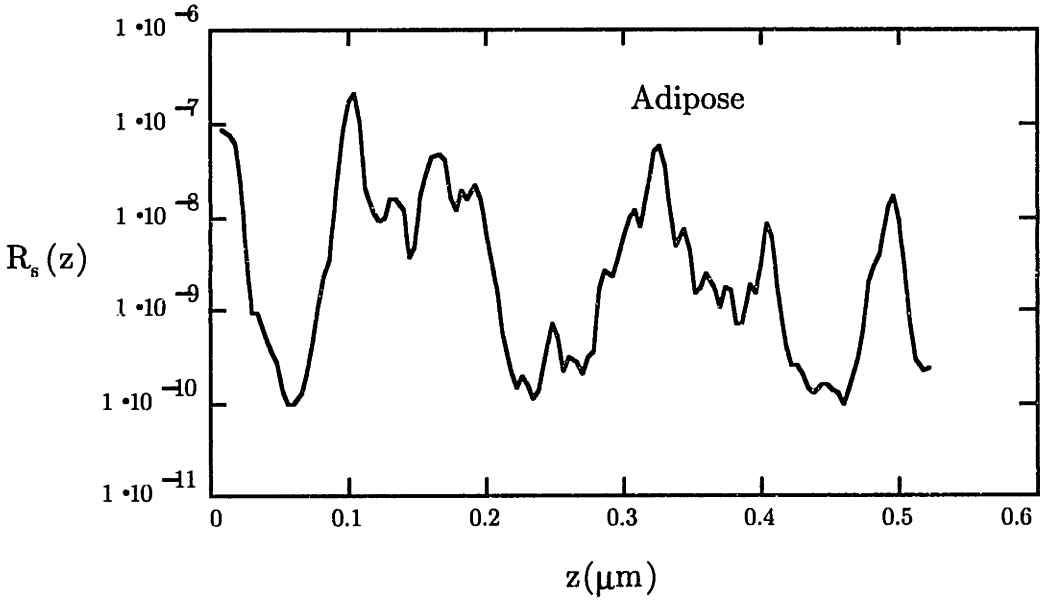

Figure 4.11. Reflectance plots for *in vitro* mesenteric adipose tissue.

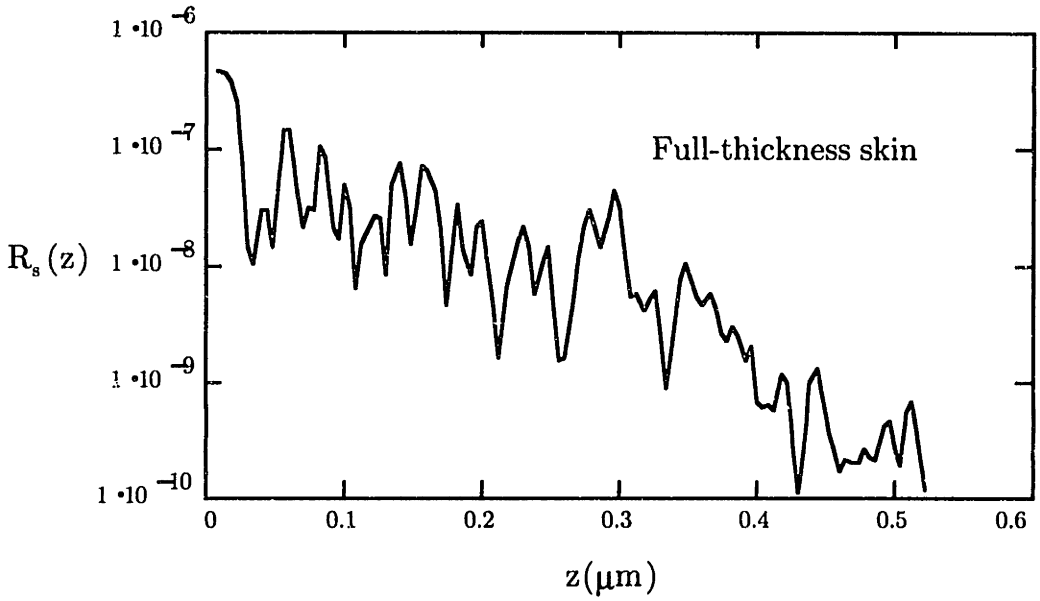

Figure 4.12. Reflectance plot for *in vitro* full-thickness human skin.

The results of the optical properties measurement using single backscatter theory are shown in Table 4.2. The results obtained from the OCT experiments are compared with estimated values of tissue optical properties obtained from the literature[20]. As can be predicted from the large negative slope of the reflectance data, the muscle attenuation and radar backscattering coefficients are much larger than that of adipose tissue. The optical properties of the full-thickness skin lie in between these two extremes.

Tissue type	Predicted μ_t (mm^{-1})	Measured μ_t (mm^{-1})	Predicted μ_b (mm^{-1})	Measured μ_b (mm^{-1})
Skin	4.0	3.92±.31	0.52	0.131±.04
Adipose	1.1	1.79±.07	3.5	0.013±.009
Muscle	3.5	5.85±.31	1.062	0.41±.075

Table 4.2 Optical properties measurements for *in vitro* human tissue specimens.

Reflectance plots calculated from single backscattering theory are shown in Figures 4.13 - 4.15. The optical properties used in the theoretical fits are taken from Table 4.2. The dotted lines depict theoretical reflectance profiles obtained by varying of the optical properties ±20 percent.

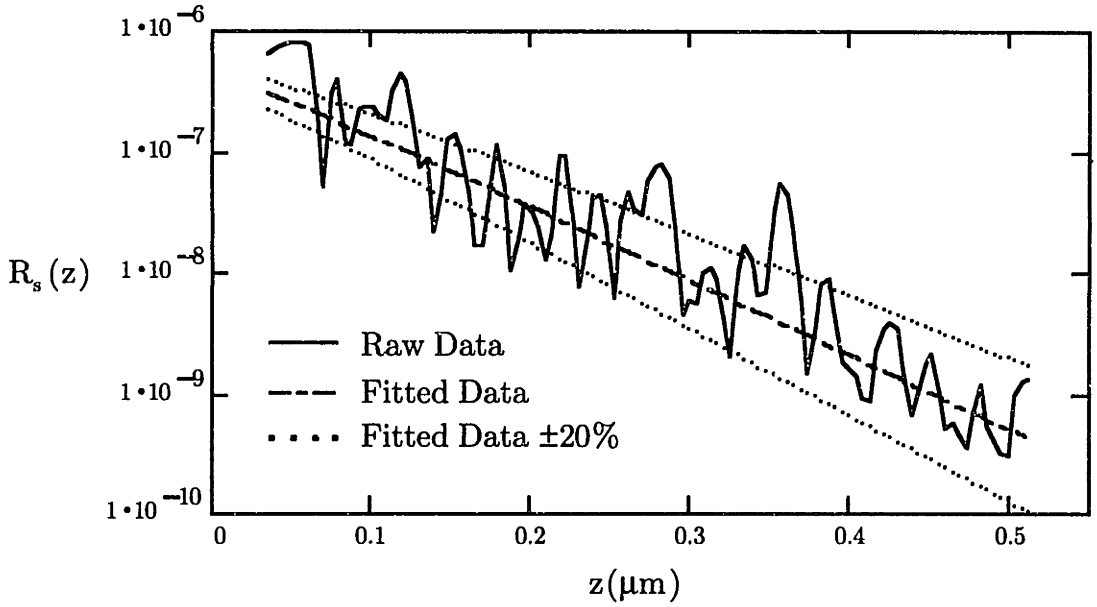

Figure 4.13. Reflectance plots for *in vitro* left ventricular muscle. Fitted data corresponds to reflectance calculated from single backscatter theory using the measured optical properties of the tissue, $\mu_t = 5.85mm^{-1}$, $\mu_b = 0.41mm^{-1}$. Dotted lines represent fitted curves for 20% variation from the measured optical properties, $\mu_t = \mu_t \mp 0.2\mu_t$ and $\mu_b = \mu_b \pm 0.2\mu_b$.

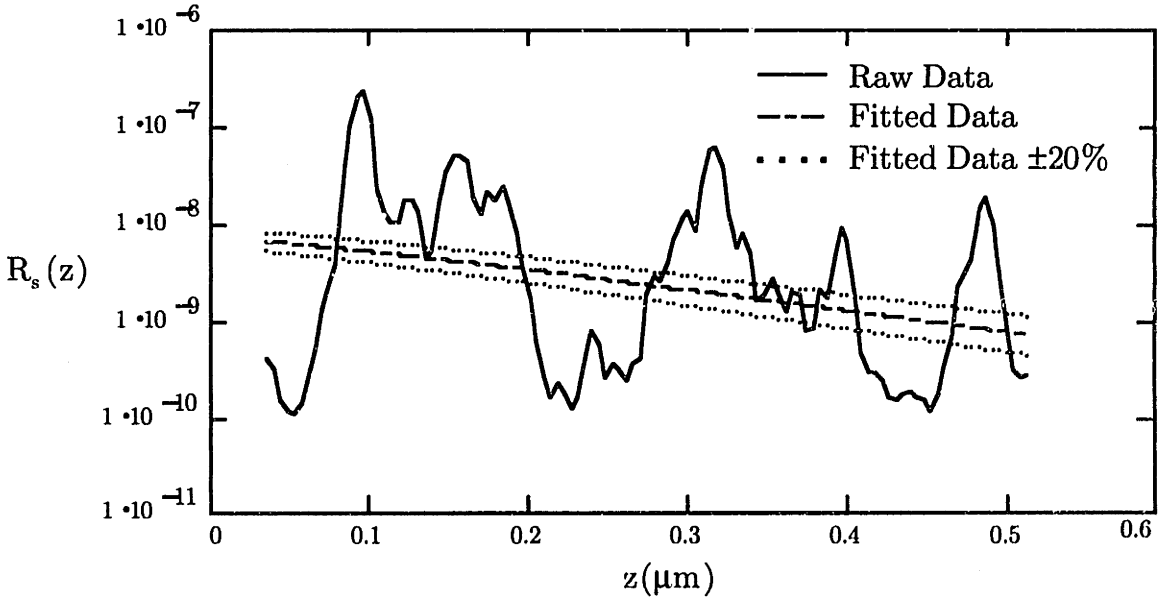

Figure 4.14. Reflectance plots for *in vitro* mesenteric adipose tissue. Fitted data corresponds to reflectance calculated from single backscatter theory using the measured optical properties of the tissue, $\mu_t = 1.79mm^{-1}$, $\mu_b = 0.013mm^{-1}$. Dotted lines represent fitted curves for 20% variation from the measured optical properties, $\mu_t = \mu_t \mp 0.2\mu_t$ and $\mu_b = \mu_b \pm 0.2\mu_b$.

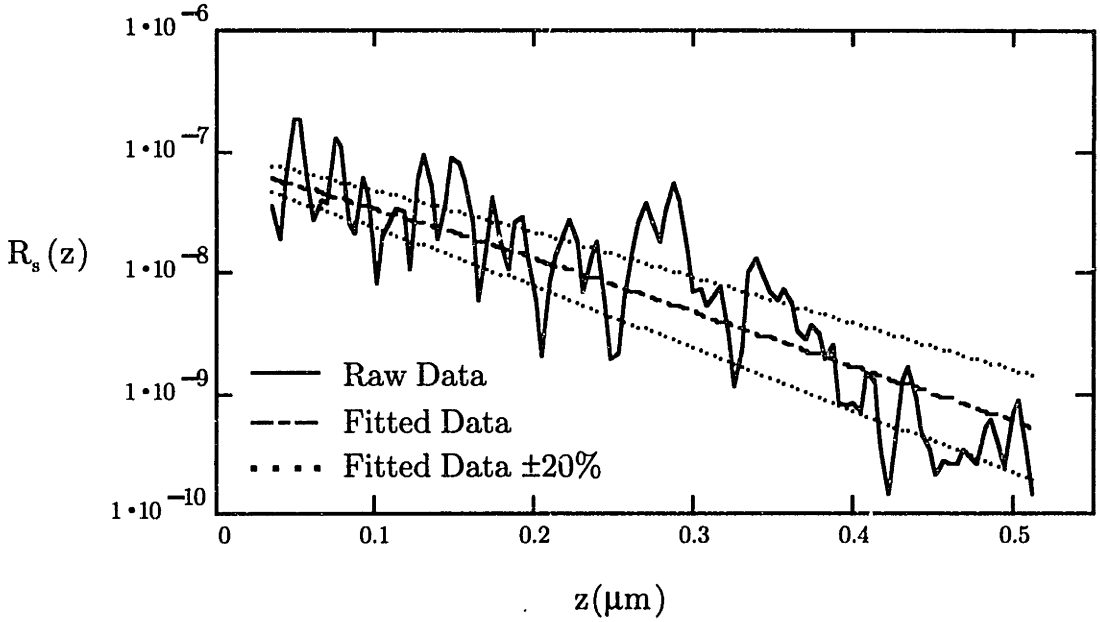

Figure 4.15. Reflectance plot for *in vitro* full-thickness human skin. Fitted data corresponds to reflectance calculated from single backscatter theory using the measured optical properties of the tissue, $\mu_t = 3.92 mm^{-1}$, $\mu_b = 0.41 mm^{-1}$. Dotted lines represent fitted curves for 20% variation from the measured optical properties, $\mu_t = \mu_t \mp 0.2\mu_t$ and $\mu_b = \mu_b \pm 0.2\mu_b$.

In vivo tissue optical properties: The reflectance profile for *in vivo* human skin is plotted in Figure 4.16. As in the *in vitro* plot, two separate decay constants are seen in the reflectance profile. These different decay constants most likely represent the epidermis and the dermis. The arrow points to the interface between these two layers of the skin. The refractive index mismatch at this interface may give rise to the reflectance peak at this point. The negative slope of the reflectance profile decreases beyond $300\,\mu m$. This decrease in negative slope is likely due to an increase in the amount of multiple scattering detected by the OCT system.

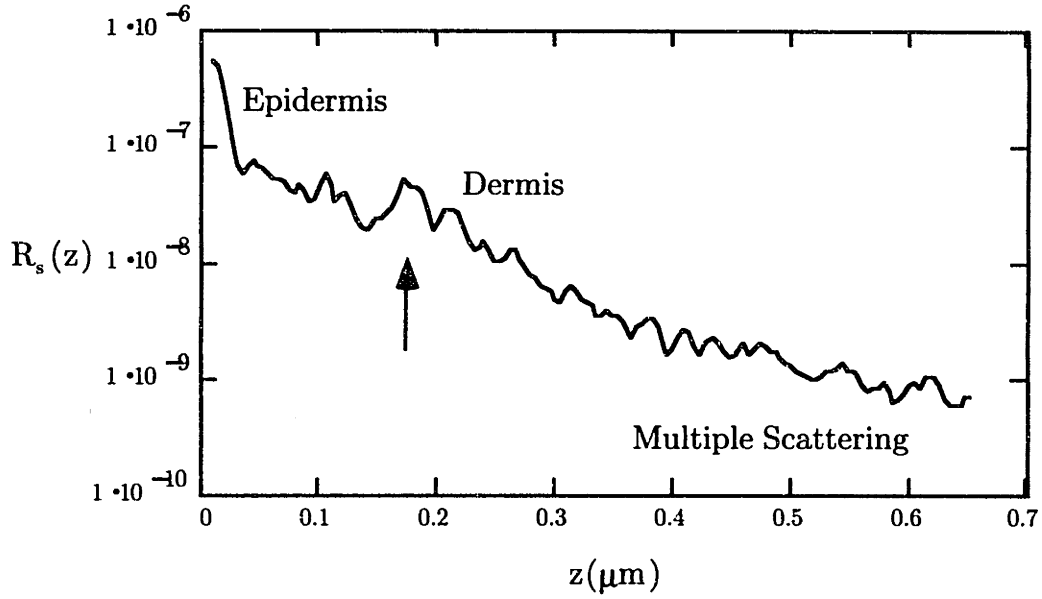

Figure 4.16. Reflectance plot for *in vivo* full-thickness human skin.

The results of the optical properties measurement using the single backscatter theory is shown in Table 4.3. The results obtained from the OCT experiments are compared with estimated values of the optical properties of *in vitro* skin obtained from the literature[20]. The radar backscattering coefficient for human skin has only been reported using the method of section 4.3[20]. No values of the radar backscattering coefficient have been reported for the human epidermis.

Tissue type	Predicted μ_t (mm^{-1})	Measured μ_t (mm^{-1})	Predicted μ_b (mm^{-1})	Measured μ_b (mm^{-1})
Epidermis	4.0	1.84±.15	Unknown	0.043±.013
Dermis	1.0	5.82±.77	1.2	0.135±.01

Table 4.3 Optical properties measurement for *in vivo* human skin.

4.5.4 Discussion

For the latex polystyrene phantoms, the results of the single backscattering theory corresponds with the optical properties of the phantoms calculated by Mie theory (Table 4.1). Single backscatter optical property measurements of *in vitro* and *in vivo* human tissue also correspond well with previously measured values of the optical properties of tissue.

The sensitivity of optical property measurement decreases with the magnitude of the optical properties (Figures 4.6 - 4.9, 4.13 - 4.15). This decrease in sensitivity is particularly noticeable when measuring the optical properties of heterogeneous tissue with relatively low backscattering and attenuation coefficients (Figure 4.14). For these samples, the optical properties determined using single backscatter theory should be interpreted with caution.

The results of the *in vitro* measurements of the optical properties aid in understanding the reflectance in OCT images. For example, the low attenuation and backscattering coefficient of adipose tissue relative to water based tissues provides a valid rationale for the differences in contrast found between fatty plaques and the surrounding intima and media in atherosclerotic aortas (Figure 4.17)[9].

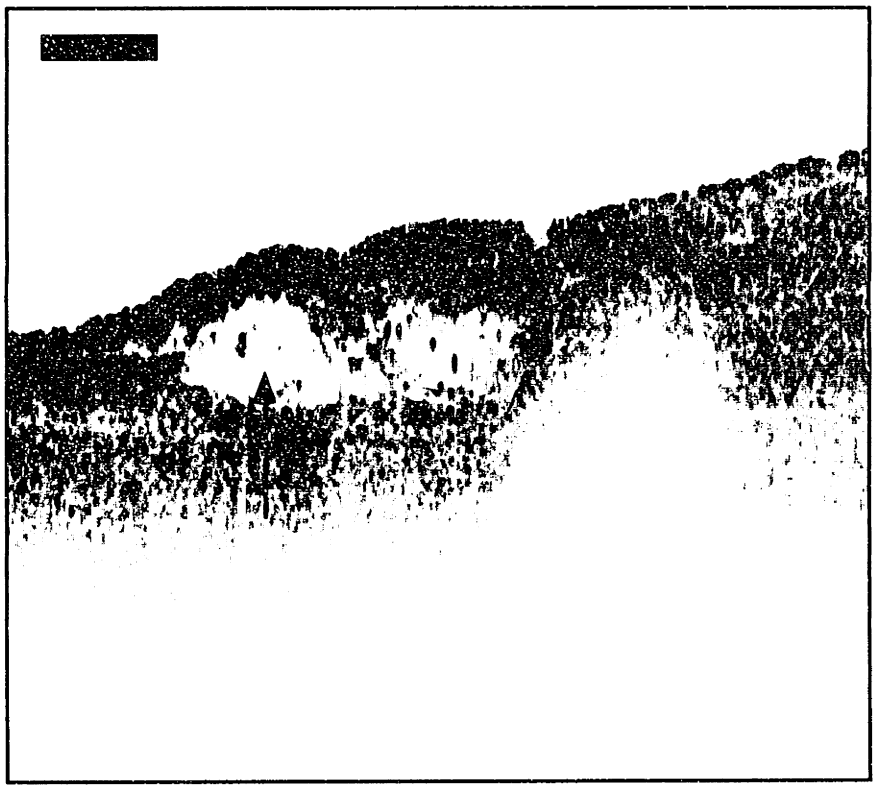

Figure 4.17. OCT image of *in vitro* human aortic atherosclerotic fatty plaque. Image was acquired at 1300 nm. Arrow points to area of adipose tissue with a relatively low backscattering and total attenuation coefficient. Bar represents 500 μm. Data is displayed as the inverse of the linear reflectance.

While the results of the single backscatter approximation are impressive at imaging depths less than 200 μm, the single backscatter method for determining the optical properties of human tissue breaks down at imaging depths greater that 200-300 μm. The inaccuracy of single backscattering theory at large depths is due to the increased detection of multiple scattering by the OCT system. Thus, the single backscatter method can only be used to measure the optical properties of human tissue at the surface.

Yet, this may not be a serious limitation. Many applications for optical property measurement in clinical medicine only require knowledge of the optical properties at the surface of the tissue. For example, irradiant dosimetry for the treatment of cancer using photodynamic therapy can be performed superficially.

Nevertheless, if a general method for determining the optical properties in tissue is to be universally accepted, the multiple scattering effects in OCT must be addressed. In addition, the effects of multiple scattering must be quantified for proper determination of depth dependent resolution in OCT images.

Chapter 5

PSF's in Turbid Media and Empirical Determination of the Multiple Scattering Limit for *In Vitro* Tissue

5.1 Introduction

Low coherence interferometry can be used to determine the optical properties of human tissue only if the OCT signal is in the single scattering limit. This assumption is only valid for imaging depths where $\mu_s z << 1$. Multiple scattering also adversely affects the resolution of OCT images. As the ratio of single scattering to multiple scattering decreases, the PSF of the OCT system broadens. This chapter describes a framework for understanding multiple scattering using the spatial mutual coherence function. In addition, an empirical determination of the decrease in resolution due to multiple scattering is presented. Empirical quantification of the resolution degradation is performed by measuring the axial point spread functions of the OCT system within phantom scattering media and human tissue.

5.2 The Spatial Mutual Coherence Function

The spatial mutual coherence function determines the degree of spatial coherence between two optical fields separated by a distance ρ in a plane perpendicular to the direction of propagation (Figure 5.1)[24].

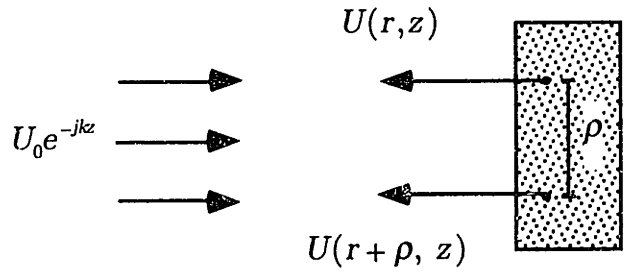

Figure 5.1. Geometry for calculating the plane wave mutual coherence function.

The spatial mutual coherence function is defined as the cross-correlation between these two optical fields[24]:

$$M(\rho,z)=\left\langle U(r,z),U^{*}(r+\rho,z)\right\rangle. \tag{5.2.1}$$

Several important limits of the mutual coherence function must be defined in order to interpret the mutual coherence function in the general case. The mutual coherence function for reflected radiation for two coincident points, $\rho=0$, is only dependent on the absorption coefficient[24]:

$$M(0,z)=\left\langle\left|U(r,z)\right|^{2}\right\rangle=U_0^2\exp(-2\mu_a z). \tag{5.2.3}$$

When $\rho\Rightarrow\infty$, radiation cannot have reached both r and $r+\rho$ without having been scattered, so

$$M(\infty,z)=\left|\left\langle U(r,z)\right\rangle\right|^{2}=U_0^2\exp(-2\mu_t z), \tag{5.2.4}$$

and the mutual coherence function is dependent on the total attenuation coefficient[24]. For this case, the mutual coherence function is independent of ρ and is equal to the unscattered attenuation of the reflected field.

The mutual coherence function for values of ρ between 0 and ∞ has been computed to be[24]:

$$M(\rho,z)=U_0^2\exp\left(-2\left[\mu_a z+\mu_s z\left(1-f(\rho)\right)\right]\right), \tag{5.2.5}$$

where for small angle scattering,

$$f(\rho)=1-\tfrac{1}{3}(1-g^{2})\pi^{2}\rho^{2}. \tag{5.2.6}$$

The heterodyne power detected by the low coherence interferometry system is proportional to the effective receiver area[25]. For a circular aperture,

$$A_{RE}(z)=2\pi\int_0^D M(\rho,z)R_0(\rho)\rho d\rho, \tag{5.2.7}$$

where $R_0(\rho)$ is the transfer function of the circular aperture and D is the beam diameter at the sample[25].

Using these formulae for the spatial mutual coherence functions for forward scattering media, the ratio of multiple to single scattered components of the interference signal can be defined as[22]:

$$S_r(z) = \frac{A_{RE,MS}}{A_{RE,SS}} = \frac{\int_0^D M(\rho,z)R_0(\rho)\rho d\rho}{\int_0^D M(\infty,z)R_0(\rho)\rho d\rho}. \tag{5.2.8}$$

Thus, the ratio of multiple to single scattering due to mutual coherence between two scatterers in the medium is dependent on the spot size, D, the anisotropy coefficient, g, and the imaging depth, z. A plot of $S_r(z)$ for different values of g, computed from Equation 5.2.8, is shown in Figure 5.2.

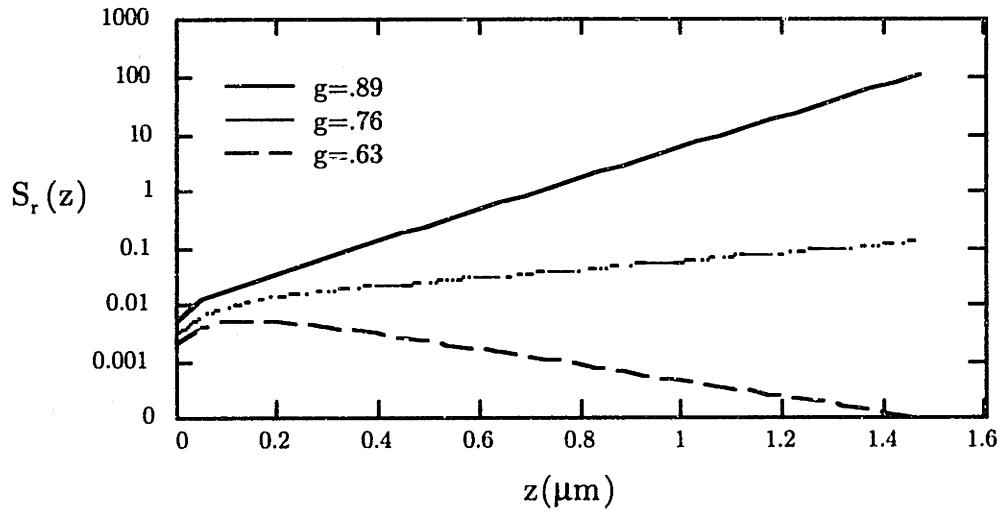

Figure 5.2. Multiple to single scattering ratio, S_r for different values of g. The spot diameter, D, at the sample is $30\,\mu m$. The total attenuation coefficient, μ_t, is 5.1 mm^{-1}.

Using this definition of the percentage of multiple scattering as a function of z and the reflectance calculated from the single backscattering theory (Section 4), single backscattering theory can be corrected to include the effects of multiple scattering due to spatial mutual coherence:

$$R_m(z) = R_s(z)\left[1 + S_r(z)\right]. \tag{5.2.9}$$

Figure 5.2 depicts the single backscatter reflectance corrected for multiple scattering.

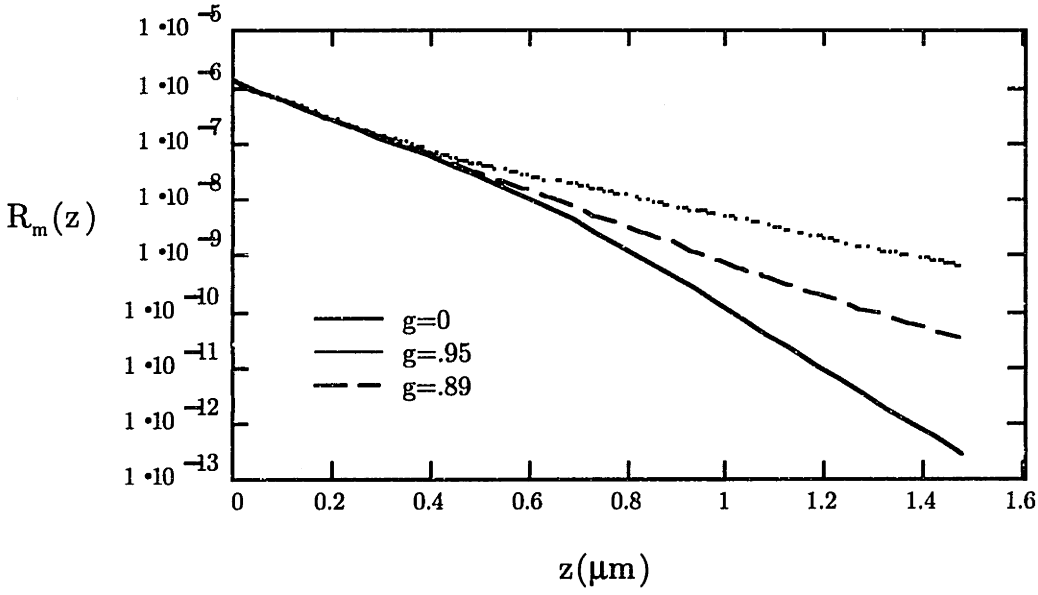

Figure 5.2. Reflectance computed using single backscatter theory corrected for multiple scattering. Values of g below 0.76 show no appreciable multiple scattering effects. The spot diameter at the sample is $30\mu m$ and the total attenuation coefficient, μ_t, is 5.1 mm^{-1}.

The decrease in negative slope shown in Figure 5.2, is also seen in the plots of reflectance obtained from the polystyrene spheres (Figure 4.4) and human tissue (Figures 4.5 - 4.8). However, the multiple scattering effects in Figure 4.5 for 0.966 μm diameter spheres ($g = 0.89, \mu_t = 5.1 mm^{-1}, D = 30\mu m$) is more severe than the effects predicted by spatial mutual coherence function calculations. In addition, multiple scattering begins to affect the OCT signal at a smaller value of z in the polystyrene phantoms (200 μm vs. 400 μm). Thus, while the small angle scattering

spatial mutual coherence function describes most of the effects of multiple scattering, other sources of multiple scattering also contribute to the OCT signal.

5.3 Measurement of OCT Axial Point Spread Functions

Since the spatial mutual coherence function only partially explains multiple scattering, other methods must be used to characterize the multiple scattering contribution to the OCT signal. The following study is an attempt to empirically determine the contribution of multiple scattering to the OCT signal by measuring the spread of the axial PSF of the OCT system as a function of depth, z.

5.3.1 Methods

System Configuration: The OCT system consists of a single mode fiber optic Michelson interferometer (Figure 2.1). A superluminescent diode with a center wavelength at 1300 nm and a spectral bandwidth of 50 nm was used for the experiments. The system used a 5x objective, resulting in an axial resolution of 20 μm and a transverse resolution of approximately 30 μm. The beam diameter was measured by scanning a razor blade and using the clipping technique[23]. The focal length was determined by knowing the beam diameter and measuring the confocal parameter, b (Equation 4.5.18). The object arm power was 100 μW, and the signal to noise ratio was 110 dB.

Sample Preparation: Phantoms were constructed using solutions of latex polystyrene microspheres in distilled H_2O. Phantoms with anisotropy coefficients at 1300 nm of 0.63, and 0.89 were prepared for spheres of 0.502 and 0.966 μm diameter. The total attenuation coefficient for both samples was 5.1 mm^{-1}. A razor blade was placed in the phantom at an angle. The optical properties of the phantoms were determined using the methods of Section 4.5. Tissue samples were taken postmortem and consisted of human full thickness skin, mesenteric adipose, and left ventricular cardiac muscle. All *in vitro* tissue samples were dissected to a thickness of 2 mm. As in the phantom samples, a razor blade was placed in the specimens at an angle. All of the tissue samples were stored in isotonic saline and immersed in sodium azide. The tissues were imaged at 100% hydration at 25°C.

Data Acquisition: The sample arm was focused on the surface of the objects to be imaged. OCT images of the samples were then acquired by scanning the reference

arm to obtain axial reflectance profiles. The stage was scanned laterally to create images of the razor blade at different depths in the media. The images were acquired with spatial dimensions of 2x6 mm. The size of the scans were 500x250 pixels. All images were averaged 4 times. The single image scan time was approximately 60 seconds.

Data Analysis: All scans were normalized by R_0. Background noise was subtracted from all scans. Fresnel reflection was removed from each scan and the z=0 data was estimated by extrapolating a log fit of the data. The radar backscattering coefficient was determined by using z=0 data and Equation 4.5.16. Data was exponentially fit up to approximately 200 μm to determine the total attenuation coefficient (Equation 4.5.17). Data was only fit up to 200 μm because this was the greatest depth at which all samples had no noticeable effects of multiple scattering. The refractive indices used in the analysis were taken from the results of Chapter 3. The axial PSF of each sample as a function of z was determined by averaging 5 vertical lines of interest at the position of the razor blade. The widths of the PSF's were computed by measuring the FWHM of the reflectance peak at the position of the razor blade.

5.3.2 Results

Phantom axial point spread functions: Images of the razor blade phantoms (μ_t= 5.1 mm^{-1}) for two values of g are shown in Figure 5.3. Multiple scattering can be seen to broaden the PSF at approximately 300 μm for $g = 0.89$. No PSF broadening can be seen in the OCT image for g = 0.63. The mirroring of the surface below the razor blade is probably due to secondary reflections from the air-sample interface.

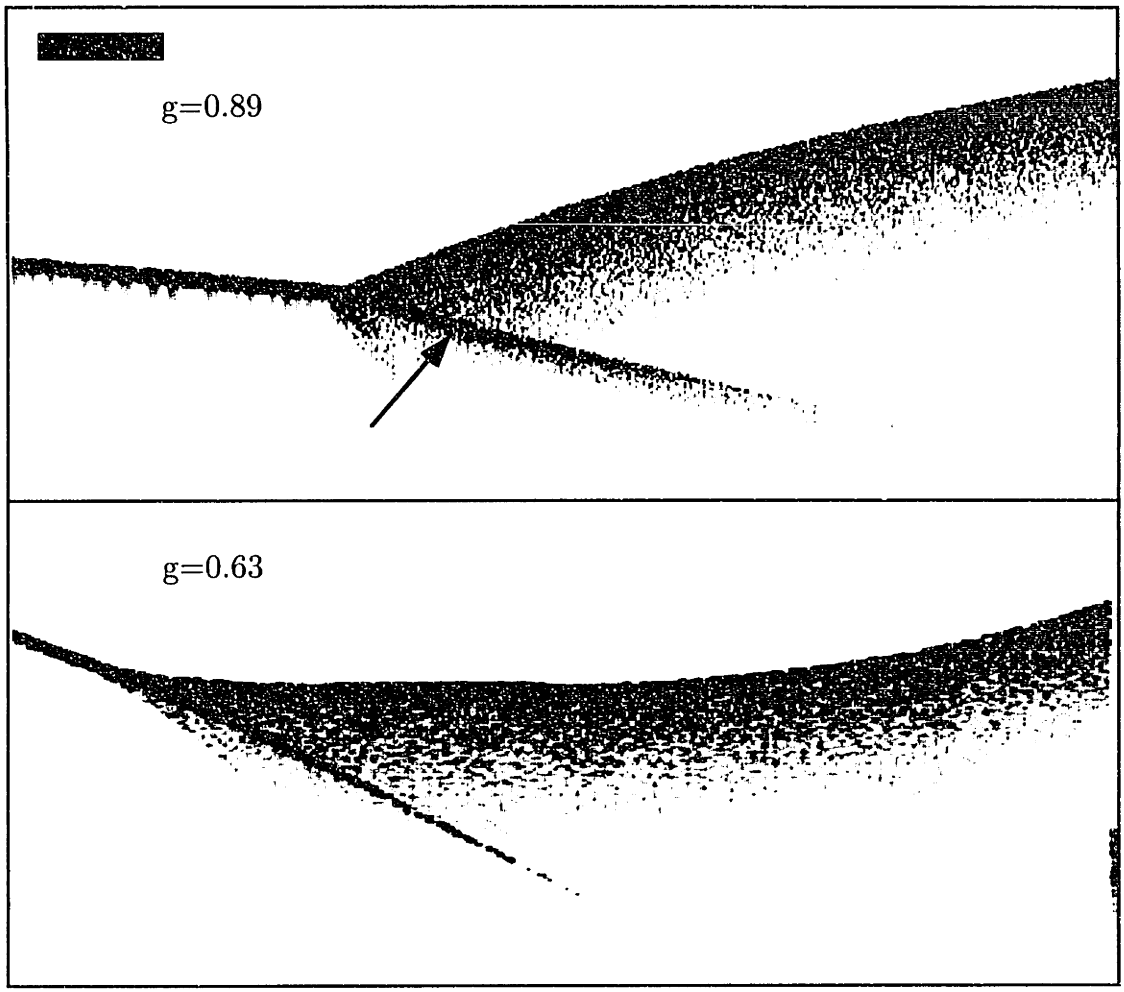

Figure 5.3. OCT images of razor blade embedded in phantoms. PSF broadening due to multiple scattering is visible in the phantom g=0.89 (Arrow). Data is displayed as the inverse of the linear reflectance. Bar represents 500 μ m.

The full width half maxima of the PSF's as a function of z are plotted for two different values of g in Figure 5.4. Both samples, $g = 0.89$ and $g = 0.63$, have a PSF FWHM of $20\mu m$ for axial positions $z < 400\mu m$. This plot shows an increase in the width of the PSF for $g = 0.89$ at approximately 400 μm. The PSF FWHM for the $g = 0.89$ sample increases to 60 μm at an axial position of 1200 μm. The FWHM for the PSF at $z = 1200$ μm for $g = 0.63$ only increases to 30 μm. This data clearly demonstrates that the ratio of multiple to single scattering in the OCT signal increases as a function of g and z.

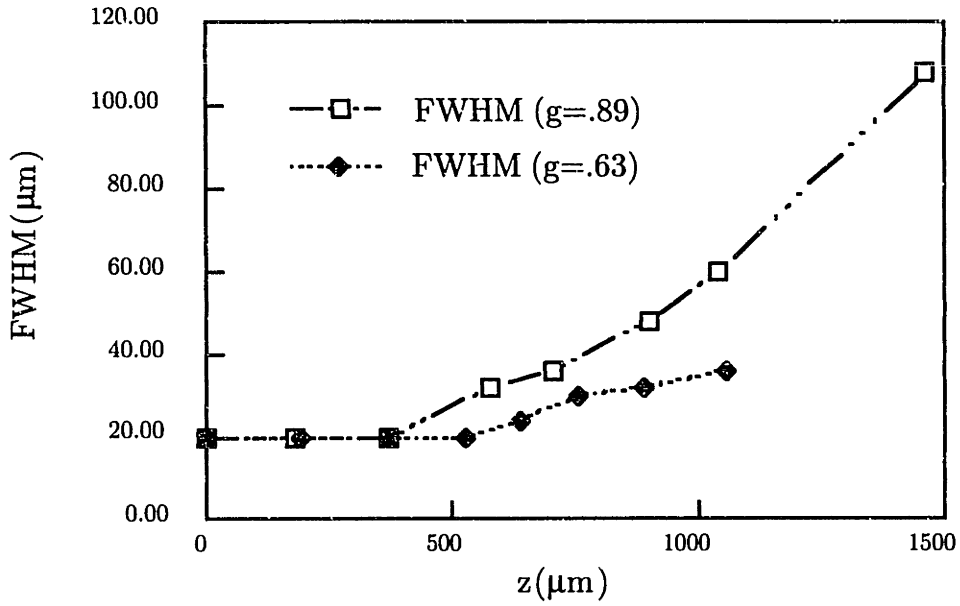

Figure 5.4. Full width half maxima of the point spread functions for latex polystyrene sphere phantoms.

In vitro tissue axial point spread functions: Images of the razor blade embedded in left ventricular muscle, mesenteric adipose tissue, and full-thickness human skin are shown in Figure 5.5. Axial spreading of the PSF occurs at $z = 800\mu m$, $200\mu m$, and $250\mu m$ in the muscle, adipose, and skin tissues, respectively.

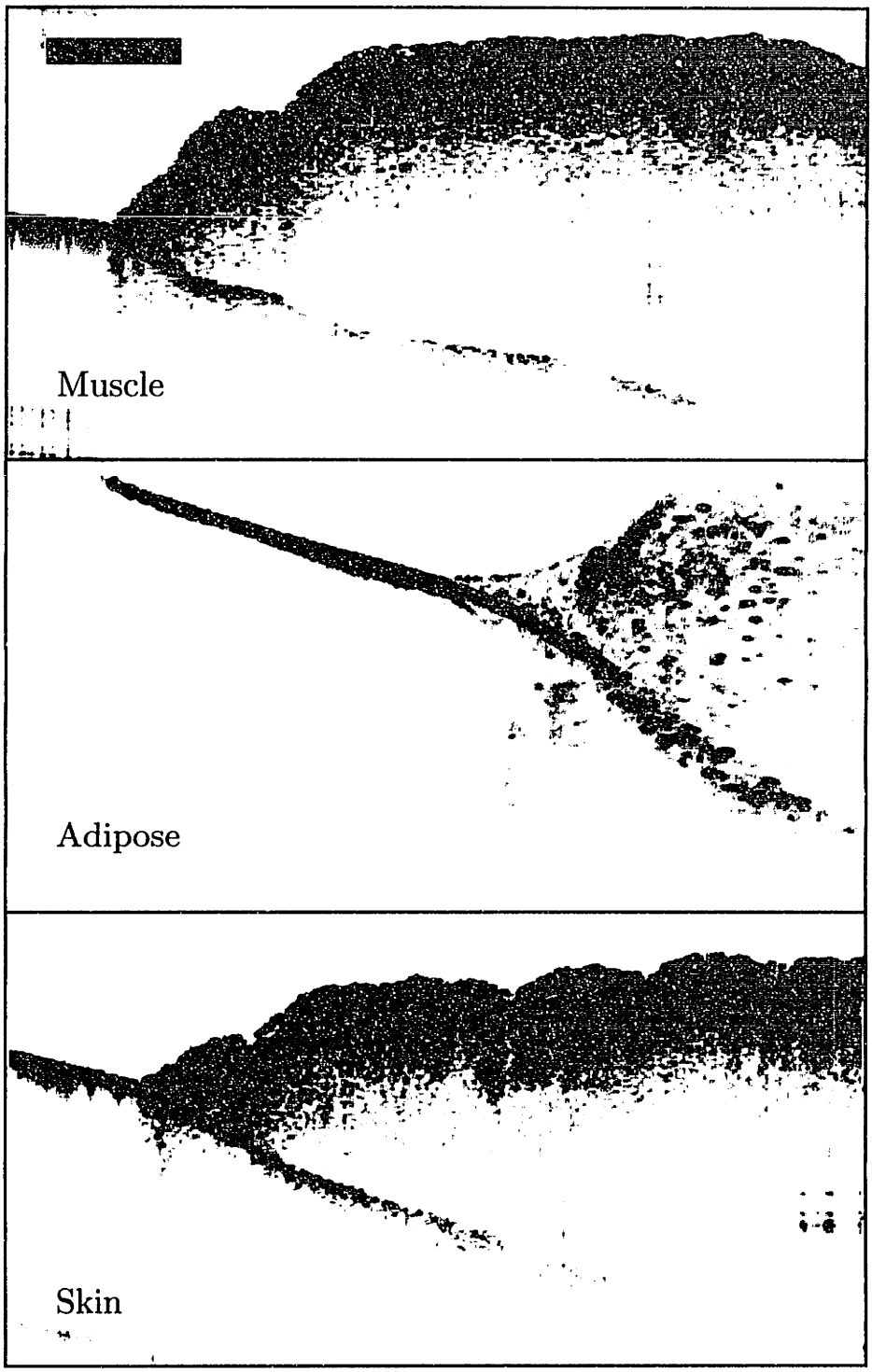

Figure 5.5. OCT images of razor blade embedded in human tissue. Data is displayed as the inverse of the linear reflectance. Bar represents 500 μ m.

The full width half maxima of the PSF's as a function of z are plotted for muscle, adipose tissue, and skin in Figure 5.6. All three samples have a PSF FWHM of $20\mu m$ for axial positions $z < 200\mu m$. This plot shows an increase in the width of the PSF at $200\mu m$, $250\mu m$, and $750\mu m$ for the adipose, skin, and muscle tissues, respectively. In addition, the PSF FWHM of the adipose tissue increases to a width of $170\mu m$ at an axial position of $1100\,\mu m$. The skin PSF width broadens to $70\mu m$ while the muscle PSF FWHM increases to only $40\mu m$ at an axial position of $1100\,\mu m$. By comparing these results with the phantom results, the scattering in adipose tissue must be highly forward directed, $g > 0.9$. The anisotropy coefficient of skin must be somewhat lower, $0.63 < g < 0.9$. The muscle anisotropy coefficient is the lowest of all three tissue types, $g < 0.63$.

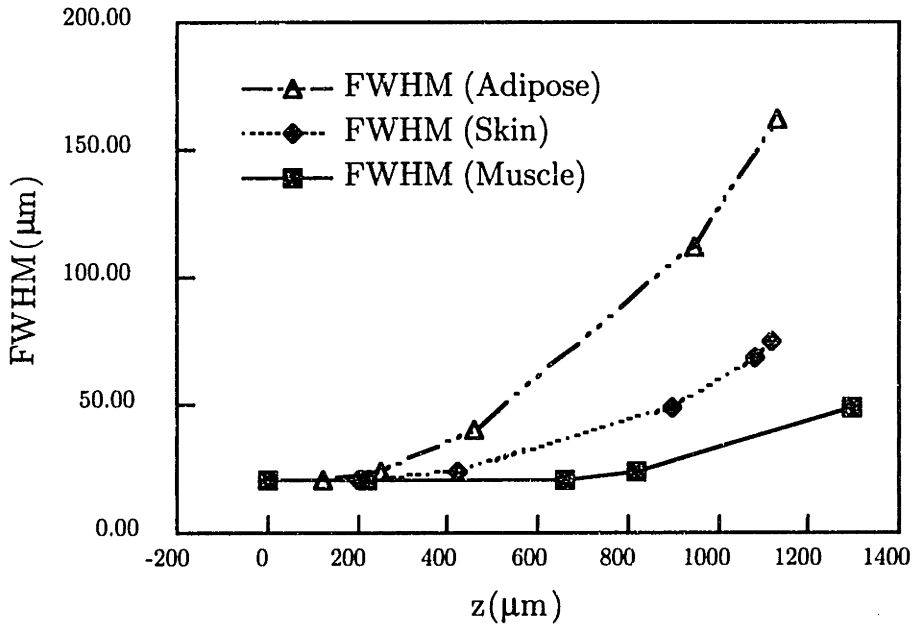

Figure 5.6 Full width half maxima of the point spread functions for human tissue specimens.

As mentioned in Section 4.3, the radar backscattering coefficient decreases as the value of g increases. Hence, the results of this experiment are consistent with the radar backscattering coefficients determined for the three tissue types using single backscatter theory (Section 4.5). The radar backscattering coefficients for the muscle, skin, and adipose were computed to be 0.41, 0.131, and 0.013 mm^{-1}, respectively.

5.3.3 Discussion

The multiple scattering contribution to the OCT signal increases with imaging depth, z, and the anisotropy coefficient, g. This effect can be empirically quantified by measuring the broadening of the PSF as a function of axial position in the sample. PSF broadening measurements show that single scattered imaging can be performed through 4 mean free paths (MFP's) for $g = 0.89$ and 5 MFP's for $g = 0.63$. These values are much lower than those found by transillumination coherence gating studies (20 MFP's)[6]. The reason for this decrease in single scattered imaging depth is primarily due to the multiple scattering effects described by the small angle scattering spatial mutual coherence function.

Since spatial mutual coherence appears to be the primary cause of multiple scattering, it may be used to place a lower limit on the ratio of multiple to single scattering for OCT. This lower limit has serious implications for using OCT to reduce multiple scattering in OCT enhanced confocal microscopy. Figure 5.7 depicts the theoretical corrected reflectance for a high numerical aperture objective incident on a phantom with $\mu_t = 5.1 mm^{-1}$, g = 0.89. This plot shows that the multiple scattering can increase the OCT signal by an order of magnitude. This could potentially broaden of the confocal PSF can by a factor of three, from 1 μm to 3 μm when focused at a depth of 300 μm. This best case PSF broadening would prohibit imaging of cellular structure for clinically relevant depths in highly scattering tissue. Studies will be performed to measure the OCT enhanced confocal axial PSF to verify these predictions.

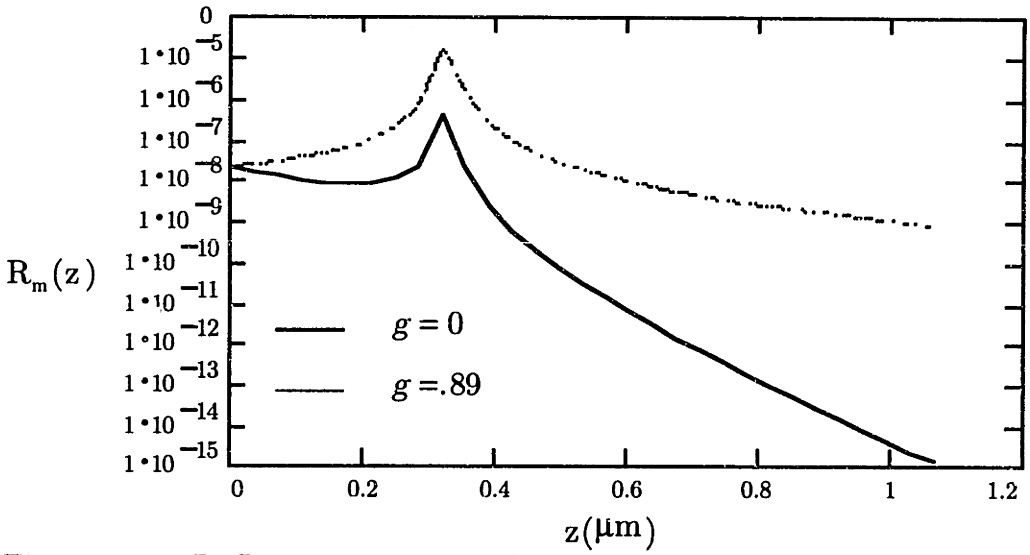

Figure 5.7. Reflectance computed using single backscatter theory corrected for multiple scattering. The plot for $g = 0$ corresponds to the reflectance obtained from the uncorrected single backscatter theory. The confocal parameter of the objective is $1\,\mu m$, corresponding to a numerical aperture of 0.7. The total attenuation coefficient, μ_t is 5.1 mm^{-1}. The multiple scattering to single scattering ratio is > 10 when the objective is focused 300 μm into the medium.

While PSF broadening as a function of increasing anisotropy coefficient is predicted by the small angle scattering mutual coherence function, it does not explain the severity of multiple scattering seen by the onset and magnitude of the decrease in negative slope in scattering phantoms (Figure 4.5). Thus, spatial mutual coherence is only one source of the multiple scattering effects seen in OCT reflectance from multiply scattering media. Future work will focus on the investigation of other sources of multiple scattering in OCT.

Chapter 6

Summary and Conclusion

Non-invasive measurement of the optical characteristics of tissue has become increasingly important due to the prevalence of optical diagnostic and treatment methods in medicine. Knowledge of the refractive index and the optical properties of tissue is essential for understanding the transport of light in tissue. Prediction of optical transport is necessary for optimization of laser treatment such as photodynamic therapy. Also, knowledge of the optical characteristics of tissue is useful for understanding high resolution images of human tissue obtained using OCT.

Two methods for measuring the refractive index of tissue using low coherence interferometry have been presented. Optical pathlength measurement using OCT produces tissue refractive index measurements that correspond to predicted values found in the literature. This method is invasive, for it requires placing the sample on a reflecting surface. Yet, it does not require tissue homogenization and thus provides a better representation of the refractive index than other available methods. Therefore, this technique should become useful for cataloguing of the refractive indices for a variety of tissue types. Moreover, the use of this method for determining the refractive index of adipose versus water based tissues provides insight into the contrast mechanisms in OCT reflectance images. Local refractive index variations between adipose and water based tissues give rise to contrast seen in human atherosclerotic plaques (Figure 4.17).

Refractive index measurement by focus tracking is a non-contact method and is therefore easily extended for use in *in vivo* human tissue. At the time of this writing, it is the only available method for determining the refractive index of multiply scattering tissue in a non-contact manner. This technique has been shown to determine the refractive index for *in vitro* human epidermis and dermis. The values determined by this method correspond well with the values presented in the literature. The applications for focus tracking include *in vivo* monitoring of tissue

hydration states and diagnosis of disease based on tissue composition changes in the refractive index.

Measurement of the total attenuation and radar backscattering coefficients in tissue has been demonstrated using a theoretical description of the OCT signal. While this method only is valid in the single scattering limit, it reliably predicts the optical properties of scattering phantoms and human tissue near the surface of the samples. There are many applications for this technique, including the determination of the absorption coefficient for the treatment of cancer with photodynamic therapy.

The results of the *in vitro* measurements of the optical properties aid in understanding the reflectance in OCT images. For example, the low attenuation and backscattering coefficient of adipose tissue relative to water based tissues provides a valid rationale for the differences in contrast found between fatty plaques and the surrounding intima and media in atherosclerotic aortas (Figure 4.17).

The effects of multiple scattering on the OCT signal are presented in Chapter 5. As predicted by the small angle scattering mutual coherence function, the FWHM of the PSF of the OCT system increases as a function of depth and g. The effects of multiple scattering has serious implications for the use of OCT enhanced confocal microscopy in highly forward scattering media. The mutual coherence function does not completely describe the effects of multiple scattering, so further work needs to be performed to characterize multiple scattering in OCT images.

To conclude, low coherence interferometry has many applications for the characterization of human tissues. Upon further development these techniques will become essential tools for researchers in the field of medical optics. In addition, the optical characteristics measured by analysis of OCT reflectance aid in understanding the OCT images. Nevertheless, work must be done to better quantify the effects of multiple scattering in order to characterize the depth dependent resolution in OCT images.

Appendix A

C Program for Calculating the Scattering Matrix of a Sphere Using Mie Theory

This program calculates $S(\theta), C_{ext}, C_b, g$. Adapted from Bohren C.F., and Huffman D.R., Absorption and Scattering of Light by Small Particles, John Wiley and Sons, New York, NY, pp. 489-490 (1983).

```
#include <stdio.h>
#include <memory.h>
#include <stdlib.h>
#include <math.h>
#include <float.h>
#include "complex.h"
#define PI 3.14159265
#define max(a,b) ((a>=b) ?a:b)

void bhmie(double x, dcomplex *refrel,long nang,dcomplex s1[],dcomplex s2[],
        double *qext,double *qsca,double *qback);


main()
{
        FILE *outfile;
        dcomplex refrel,s1[200],s2[200];
        char filename[128];
        double dia,wavel,refmed,refre;
        double rad;
        double refim;
        double x;
        long nang;
        double dang;
        double xs;
        double s11nor,sumcoss11, sums11;
        long nan;
        long    aj,j;
        double s11,s12,s33,s34;
        double pol,cosang;
        double g;
        dcomplex temp;
        double qext,qback,qsca;
        double ang;


        printf("Input medium and sphere refractive indices:");
```

```
        scanf("%lf %lf", &refmed,&refre );
        printf("Input sphere diameter, vacuum wavelength in microns:");
        scanf("%lf %lf", &dia,&wavel);
        printf("Enter output file name:");
        scanf("%s",filename);

        if( (outfile = fopen( filename, "wt" )) == NULL )
            {
            printf( "Can't open output file..." );
            exit( 1 );
            }


        printf("\n*** Sphere Scattering Program **\n");

        rad=dia/2.0;
        refim=0.0;
        refrel.r=refre/refmed;
        refrel.i=refim/refmed;
        printf("REFMED = %8.4lf, REFRE = %14.6e, REFIM =
%14.6e\n",refmed,refre,refim);
        x=2.0*PI*rad*refmed/wavel;
        printf("Sphere Radius = %7.3lf, Wavelength = %7.3lf\n",rad,wavel);
        printf("Size Parameter = %8.3lf\n",x);

        nang=46L;
        dang=PI/((double)(nang-1)*2.0);
        bhmie(x,&refrel,nang,s1,s2,&qext,&qsca,&qback);
        printf("QSCA = %13.6e, QEXT = %13.6e, QBACK = %13.6e\n",qext,qsca,qback);

        xs=qsca*PI*(rad*rad)*1e-8;
        printf("Scattering cross section = %lf\n",xs);

        s11nor=0.5*(DCabs(s2[1])*DCabs(s2[1])+DCabs(s1[1])*DCabs(s1[1]));
        nan=2*nang-1;
        sumcoss11=0.0;
        sums11=0.0;
        printf("Angle\tRe(s1)\tIm(s1)\tRe(s2)\tIm(s2)\n");
        fprintf(outfile,"Angle\tRe(s1)\tIm(s1)\tRe(s2)\tIm(s2)\n");
        for (j=1;j<=nan;j++)
         {
      aj=j;
      s11=0.5*DCabs(s2[j])*DCabs(s2[j]);
      s11=s11+0.5*DCabs(s1[j])*DCabs(s1[j]);
      s12=0.5*DCabs(s2[j])*DCabs(s2[j]);
      s12=s12-0.5*DCabs(s1[j])*DCabs(s1[j]);
      pol=-s12/s11;
      temp = DCmul(s2[j],DCconj(s1[j]));
      s33 = temp.r;
      s33=s33/s11;
      s34=temp.i;
      s34=s34/s11;
      s11=s11/s11nor;
      ang=dang*(aj-1.0)*57.2958;
```

```
        cosang=cos(ang/57.2958);
        sumcoss11=sumcoss11+cosang*s11;
        sums11=sums11+s11;
        printf("%lf\t%lf\t%lf\t%lf\t%lf\n",ang,s1[j].r,s1[j].i,s2[j].r,s2[j].i);
        fprintf(outfile,"%lf\t%lf\t%lf\t%lf\t%lf\n",ang,s1[j].r,s1[j].i,s2[j].r,s2[j].i);
           }
        fclose(outfile);
        g=sumcoss11/sums11;
        printf("\nAnisotropy g = %lf\n",g);
}



void bhmie(double x, dcomplex *refrel,long nang,dcomplex s1[],dcomplex s2[],
           double *qext,double *qsca,double *qback)
{
    dcuble amu[100],theta[100],pi[100],tau[100],pi0[100],pi1[100];
    dcomplex *d;
    dcomplex y,xi,xi0,xi1;
    long double psi0,psi1,apsi0,apsi1,psi,apsi,dn,dx;
    double xstop;
    long nstop;
    double ymod;
    double dang;
    long j,jj,nmx,nn;
    dcomplex rnr,temp;
    double fn,rn;
    double chi0,chi1;
    dcomplex an,bn;
    double p,t;
    long n;
    double chi;

    d = (dcomplex *)malloc( 3000*sizeof(dcomplex) );
    if (d==NULL) {printf("Could not allocate d matrix\n"); return;}
    dx=(long double)x;
    y = DComplex((double)(x*refrel->r),(double)(x*refrel->i));

    xstop=x+4.0*pow(x,0.3333)+2.0;
    nstop=(long)(xstop);
    ymod=DCabs(y);
    /* amax 1 ? */

    nmx=(long)(max(xstop,ymod))+15;
    dang=1.570796327/(float)(nang-1);
    for (j=1;j<=nang;j++)
        {
        theta[j]=((float)j-1.0)*dang;
        amu[j]=cos(theta[j]);
        }
    d[nmx]=DComplex(0.0,0.0);
    nn=nmx-1;
    for (n=1;n<=nn;n++)
```

```
        {
      rn=nmx-n+1;
      rnr = DComplex((double)rn,0.0);
         temp = DComplex(1.0,0.0);
         d[nmx-n]=DCsub(DCdiv(rnr,y) , DCdiv( temp, DCadd(d[nmx-
n+1],DCdiv(rnr,y)) ) );
        }
    for (j=1;j<=nang;j++)
        {
      pi0[j]=0.0;
         pi1[j]=1.0;
        }

    nn=2*nang-1;
    for (j=1;j<=nn;j++)
        {
      s1[j]=DComplex(0.0,0.0);
      s2[j]=DComplex(0.0,0.0);
        }

    psi0=cos((double)dx);
    psi1=sin((double)dx);
    chi0=-sin(x);
    chi1=cos(x);
    apsi0=psi0;
    apsi1=psi1;
    xi0=DComplex(apsi0,-chi0);
    xi1=DComplex(apsi1,-chi1);
    *qsca=0.0;
    n=1;
rc:
    dn=(double)n;
    rn=(double)n;
    fn=(2.0*rn+1.0)/(rn*(rn+1.0));
    psi=(2.0*dn-1.0)*psi1/dx-psi0;
    apsi=psi;
    chi=(2*rn-1.0)*chi1/x-chi0;
    xi=DComplex(apsi,-chi);

an=DCsub(DCmul(DCadd(DCdiv(d[n],*refrel),DComplex(rn/x,0.0)),DComplex(apsi,0.
0)),DComplex(apsi1,0.0));
    an=DCdiv(an,
DCsub(DCmul(DCadd(DCdiv(d[n],*refrel),DComplex(rn/x,0.0)),xi),xi1) );

bn=DCsub(DCmul(DCadd(DCmul(d[n],*refrel),DComplex(rn/x,0.0)),DComplex(apsi,
0.0)),DComplex(apsi1,0.0));
    bn=DCdiv(bn,
DCsub(DCmul(DCadd(DCmul(d[n],*refrel),DComplex(rn/x,0.0)),xi),xi1) );
    *qsca=*qsca+(2.0*rn+1.0)*(DCabs(an)*DCabs(an)+DCabs(bn)*DCabs(bn));
    for (j=1;j<=nang;j++)
        {
      jj=2*nang-j;
      pi[j]=pi1[j];
      tau[j]=rn*amu[j]*pi[j]-(rn+1.0)*pi0[j];
```

```
      p=pow(-1.0,(double)(n-1));
      s1[j]=DCadd(s1[j],

DCmul(DComplex(fn,0.0),DCadd(DCmul(an,DComplex(pi[j],0.0)),DCmul(bn,DComple
x(tau[j],0.0)))) );
      t=pow((-1.0),(double)n);
      s2[j]=DCadd(s2[j],

DCmul(DComplex(fn,0.0),DCadd(DCmul(an,DComplex(tau[j],0.0)),DCmul(bn,DCompl
ex(pi[j],0.0)))) );
      if(j==jj) break;
       s1[jj]=DCadd(s1[jj],
          DCmul(DComplex(fn,0.0),
          DCadd(DCmul(DCmul(an,DComplex(pi[j],0.0)),DComplex(p,0.0)),
          DCmul(DCmul(bn,DComplex(tau[j],0.0)),DComplex(t,0.0)))));
       s2[jj]=DCadd(s2[jj],
          DCmul(DComplex(fn,0.0),
          DCadd(DCmul(DCmul(an,DComplex(tau[j],0.0)),DComplex(t,0.0)),
          DCmul(DCmul(bn,DComplex(pi[j],0.0)),DComplex(p,0.0)))));
        }

    psi0=psi1;
    psi1=psi;
    apsi1=psi1;
    chi0=chi1;
    chi1=chi;
    xi1=DComplex(apsi1,-chi1);
    n=n+1;
    rn=(double)n;
    for (j=1;j<=nang;j++)
        {
      pi1[j]=((2.0*rn-1.0)/(rn-1.0))*amu[j]*pi[j];
      pi1[j]=pi1[j]-rn*pi0[j]/(rn-1.0);
         pi0[j]=pi[j];
        }
    if ((n-1-nstop) != 0) goto rc;
    *qsca=(2.0/(x*x))* *qsca;
    *qext=(4.0/(x*x))*s1[1].r;
    *qback=(4.0/(x*x))*DCabs(s1[2*nang-1])*DCabs(s1[2*nang-1]);
    free(d);
    return;
}
```

References

1. S. Hell, G. Reiner, C. Cremer and E. H. K. Stelzer, "Aberrations in confocal fluorescence microscopy induced by mismatches in refractive index," J. Microscopy **169**, 391-405 (1993).

2. D. Huang, E. A. Swanson, C. P. Lin, J. S. Schuman, W. G. Stinson, W. Chang, M. R. Hee, T. Flotte, K. Gregory, C. A. Puliafito and J. G. Fujimoto, "Optical Coherence Tomography," Science **254**, 1178-1181 (1991).

3. H. A. Haus, *Waves and Fields in Optoelectronics,* Prentice-Hall, Englewood Cliffs, New Jersey (1984).

4. B. E. A. Saleh, M. C. Teich, *Fundamentals of Photonics*, John Wiley and Sons, New York (1991).

5. T. Wilson, *Confocal Microscopy*, Academic Press, California (1990).

6. M. R. Hee, "Biological imaging with low coherence optical interferometry," Master's thesis, Massachusetts Institute of Technology, Cambridge, MA (1992).

7. M. R. Hee, J. A. Izatt, J. M. Jacobson and J. G. Fujimoto, "Femtosecond transillumination optical coherence tomography," Opt. Lett. **18**, 950-952 (1993).

8. J. A. Izatt, M. R. Hee and G. M. Owen, "Optical coherence microscopy in scattering media," Opt. Lett. **19**, 590-592 (1993).

9. M. B. Brezinski, G. J. Tearney, B. E. Bouma, J. A. Izatt, M. R. Hee, E. A. Swanson, J. S. Southern, and J. G. Fujimoto, "Optical coherence tomography for optical biopsy properties and demonstration of pathology," submitted for publication (1995).

10. F. P. Bolin, L. E. Preuss, R. C. Taylor and R. J. Ference, "Refractive index of some mammalian tissues using a fiber optic cladding method," Appl. Opt. **28**, 2297-2302 (1989).

11. T. Gahm and S. Witte, "Measurement of the optical thickness of transparent tissue layers," J. Microscopy **141**, 101-110 (1986).

12. R. R. Anderson and J. A. Parrish, "The optics of human skin," J. Investig. Derm. **77**, 13-19 (1981).

13. C. F. Bohren, D. R. Huffman, *Absoprtion and Scattering of Light by Small Particles*, John Wiley and Sons, New York (1983).

14. W. F. Cheong, S. A. Prahl, A. J. Welch, "A review of the optical properties of biological tissues", IEEE J. Quant. Elect. **26**, 2166-87 (1991).

15. A. E. Profio and D. R. Doiron, "Transport of light in tissue in photodynamic therapy of cancer," Photoch. and Photobiol. **46**, 591-599 (1987).

16. B. C. Wilson and M. S. Patterson, "The physics of photodynamic therapy," Phys. Med. Biol. **31**, 327 - 360 (1986).

17. M. S. Patterson, E. Schwartz and B. C. Wilson, "Quantitative reflectance spectrophometry for the noninvasive measurement of photosensitizer concentration in tissue during photodynamic therapy," SPIE **1065**, 115-122 (1989).

18. M. S. Patterson, B. Chance and B. C. Wilson, "Time resolved reflectance and transmittance for the non-invasive measurement of tissue optical properties," Appl. Opt. **28**, 2331-2336 (1989).

19. B. Chance, *Photon Migration in Tissues*, Plenum Press, New York (1988).

20. J. M. Schmitt, A. Knuttel and R. F. Bonner, "Measurement of optical properties of biological tissues by low coherence tissues by low-coherence reflectometry," App. Opt. **32**, 6032-6042 (1993).

21. C. M. Sonnenschein and F. A. Horrigan, "Signal-to-noise relationships for coaxial systems that heterodyne backscatter from the atmosphere," Appl. Opt. **10**, 1600-1604 (1971).

22. J. M. Schmitt, A. Knuttel, A. Gandjbakche and R. F. Bonner, "Optical characterization of dense tissues using low-coherence interferometry," SPIE **1889**, 197-211 (1993).

23. A. E. Siegman, M. W. Sasnett and T. F. Johnston, Jr., "Choice of clip levels for beam width measurements using knife-edge techniques," IEEE J. Quant. Elect. **27** 1098-1104 (1991).

24. R. F. Lutomirski, "Atmospheric degradation of electrooptical system performance," Appl. Opt. **17**, 3915-3921 (1978).

25. L. G. Kazovsky, N. S. Kopeika, "Heterodyne detection through rain, snow, and turbid media: effective receiver size at optical through millimeter wavelengths," Appl. Opt. **22**, 706-710 (1983).